Construction and Building Materials 453 (2024) 138985

Contents lists available at ScienceDirect

Construction and Building Materials

journal homepage: www.elsevier.com/locate/conbuildmat

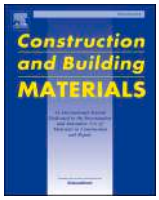

Experimental and modelling analysis of waste material-based geopolymer concrete incorporated with crumb rubber particles

Ashwin Narendra Raut [a], Ahmad Alyaseen [b], Haytham F. Isleem [c,d,*], Mohammed Rihan Maaze [e], Afzal Husain Khan [f], Arunava Poddar [b], Ahmed Salih Mohammed [g], Parveen Sihag [h]

[a] Department of Civil Engineering, Koneru Lakshmaiah Education Foundation, Vaddeswaram, India
[b] Civi, Engineering Department, Shoolini University, Solan, Himachal Pradesh 173229, India
[c] Department of Computer Science, University of York, York YO10 5DD, United Kingdom
[d] Jadara University Research Center, Jadara University, Irbid, Jordan
[e] School of Engineering NICMAR University Pune, Maharashtra 411045, India
[f] Civil and Architectural Engineering Department, College of Engineering and Computer Sciences, Jazan University, PO Box. 706, Jazan 45142, Saudi Arabia
[g] Civil Engineering Department, College of Engineering, University of Sulaimani, Kurdistan, Iraq
[h] Civil Engineering Department, Chandigarh University, Mohali, Punjab 140413, India

ARTICLE INFO

Keywords:
Geopolymer concrete
Rubberized geopolymer concrete
Microstructural properties
Soft-computing techniques
Sensitivity analysis
Economic viability

ABSTRACT

Rubberized geopolymer concrete (RuGPC) emerges as an eco-friendly alternative to conventional concrete, significantly reducing greenhouse gas emissions. This study investigates the use of steel slag (SS) in varying proportions (30 %, 35 %, and 40 %) as a replacement for ground granulated blast furnace slag (GGBS) in geopolymer concrete, with crumb rubber (CR) replacing crusher dust (CD) as fine aggregate due to its increasing demand. The research focuses on understanding the impact of aluminosilicate materials on the mechanical, thermal, and microstructural properties of geopolymer concrete cured at 60°C. Advanced characterization techniques, including Scanning Electron Microscopy (SEM), Energy-Dispersive X-ray Spectroscopy (EDX), X-ray Diffraction (XRD), and Fourier Transform Infrared Spectroscopy (FTIR), were employed. SEM and EDX analyses revealed that the microstructural properties of GGBS and SS materials, mainly Na/Si, Si/Al, H_2O/Na_2O, and Na/Al ratios, significantly influence RuGPC performance through gel formation. FTIR analysis indicates a shift in the stretching vibrations of GGBS and SS to lower wavenumbers due to geopolymerization changes. XRD results show the formation of C-S-H gel at around 27–30° 2theta, attributed to increased GGBS and SS content. Despite efforts to incorporate CR into geopolymer matrices, challenges in mitigating strength degradation persist. To address this, a predictive model was developed to understand the key factors affecting RuGPC performance. Six machine learning techniques—M5P (pruned and unpruned), random forest, random tree, linear regression, and support vector machine with various kernels (PUK, RBF, PK, and NPK), and artificial neural network (ANN)—were employed to predict the physical and thermal behavior of RuGPC. The analysis identified ANN-based models as the most effective. Sensitivity analysis highlighted the grade of rubber and the CR replacement percentage by volume of CD as the most influential parameters determining RuGPC compressive strength, density, and thermal conductivity. Moreover, The economic analysis revealed that RuGPC mixtures were 1.2–11.61 % more cost-effective than OPC concrete. These findings underscore the importance of predictive model development in optimizing RuGPC properties for practical applications, offering valuable insights for decision-making processes.

* Corresponding author at: Department of Computer Science, University of York, York YO10 5DD, United Kingdom.
E-mail addresses: ashwin7588@gmail.com (A.N. Raut), ahmd.yaseen1993@gmail.com, ahmadsarhan@shooliniuniversity.com (A. Alyaseen), mps565@york.ac.uk, isleemhaytham88@gmail.com (H.F. Isleem), rihanmaaz@gmail.com (M.R. Maaze), ahkhan@jazanu.edu.sa (A.H. Khan), arunava.nithrs@gmail.com (A. Poddar), ahmed.mohammed@univsul.edu.iq (A.S. Mohammed), parveen12sihag@gmail.com (P. Sihag).

https://doi.org/10.1016/j.conbuildmat.2024.138985
Received 26 August 2024; Received in revised form 22 October 2024; Accepted 29 October 2024

1. Introduction

1.1. Background

Concrete plays a crucial role in the construction industry worldwide, being fundamental to infrastructure development and serving as a benchmark for national progress. However, its production, which relies heavily on energy-intensive raw materials, presents significant environmental challenges [1,2]. Among these materials, natural resource-derived aggregates are indispensable, yet their increasing scarcity and rising costs pose substantial difficulties for the construction sector [3].

Geopolymer concrete (GPC) has emerged as an innovative and eco-friendly material, providing an alternative to conventional Portland cement (OPC) concrete. This material is produced through the alkali activation of aluminosilicate materials. [4]. As depicted in Fig. 1(a), the interest in GPC has surged in recent years. Unlike traditional cement concrete, GPC employs industrial by-products such as fly ash (FA), ground granulated blast furnace slag (GGBS), steel slag (SS), silica fume (SF), rice husk ash (RHA), palm oil fuel ash (POFA) and metakaolin (MK). This substitution significantly reduces greenhouse gas emissions and reliance on non-renewable resources [5]. The synthesis of geopolymer involves the activation of aluminosilicate materials with an alkaline solution, typically a mixture of sodium or potassium silicates and hydroxides [6]. This process forms a three-dimensional aluminosilicate network, which imparts superior mechanical properties and durability to the concrete, as shown in Fig. 1(b).

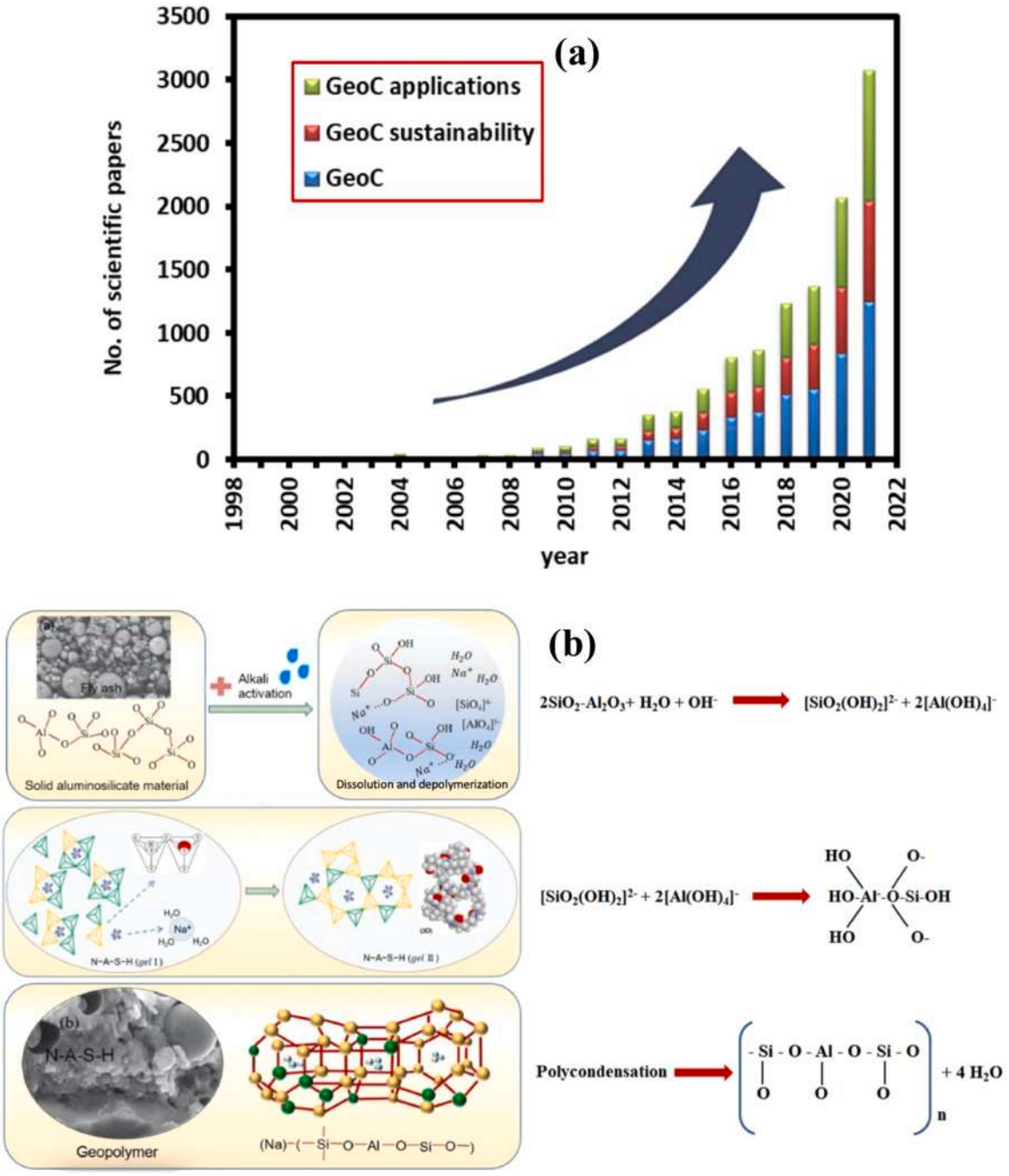

Fig. 1. (a) Articles published in ScienceDirect database [5] (b) A schematic representation of the reaction process for geopolymers created using high Si and Al and low Ca content [7].

1.2. Rubberized concrete and cementitious materials

The construction industry is facing a significant challenge due to the scarcity of sand, a primary fine aggregate, largely caused by unsustainable river mining practices. Biernacki et al. highlighted this issue [8] and emphasized that it leads to severe environmental issues such as erosion, aquifer salination, loss of storm surge protection, and a decline in biodiversity [9]. Although regulatory efforts are in place, sand demand surpasses supply, impeding economic growth. Researchers have proposed using crumb rubber (CR) from waste tires as a partial substitute for fine aggregates to address this issue. The rapid growth of the automotive industry has compounded the problem of tire disposal, with only a small fraction of end-of-life tires being recycled [10]. By crushing these tires into fine particles (0.1 mm to 4.76 mm), CR becomes suitable for use in construction, offering both environmental and functional benefits [11].

Studies on CR integration into concrete consistently reveal that increasing CR content negatively impacts concrete's mechanical properties [12–15]. with larger CR particles, leading to greater reductions in strength. However, fine CR particles perform better in terms of mechanical properties than coarse ones [16,17]. Various techniques to mitigate these negative effects have been explored, including adjusting CR particle sizes [18,19], varying CR content [20,21], and applying treatments such as soaking, washing, and coating CR aggregates [22,23] [24]. One notable benefit of CR incorporation is its low thermal conductivity (TC), which limits heat flow and enhances thermal insulation performance. However, the thermal properties of CR in cementitious materials are not well-explored. Wang et al. [25] found that CR enhances thermal performance, with studies showing a decrease in TC as CR content increases [26] [27]. This reduction is attributed to the insulating properties of rubber, air entrapment, and increased porosity in the concrete mixture [28].

With sustainability and thermal efficiency in mind, researchers have focused on developing GPC, which avoids cement as a binder. Geopolymers are considered sustainable and offer better mechanical properties than traditional cement-based binders. Incorporating CR into geopolymer concrete (RuGPC) has shown potential for enhancing ductility, impact resistance, and thermal properties [16,23] [29] [17,22, 23]. Aly [22] found that rubber aggregates improve the toughness and impact resistance of GPC. Benazzouk [26] demonstrated that rubber aggregates enhance GPC durability against freezing and thawing damage. Studies have demonstrated that replacing natural sand with CR in RuGPC results in comparable performance to conventional rubber concrete, with fine rubber particles having less impact on compressive strength (CS) than coarse particles [13,14] [18]. However, the commercialization of geopolymer technology is challenged by the variability in raw materials, which significantly affects performance. The chemical composition and physical properties of source materials such as FA, GGBS, RHA, and POFA vary greatly, requiring different activator dosages and processing methods for consistent results [30]. The integration of CR into GPC not only promotes sustainable construction by reducing waste but also conserves natural resources. GGBS, a key component of GPC, improves mechanical properties by increasing the amorphous silica and alumina content. Studies have shown that different grades of GGBS (80, 100, and 120) can be blended with FA to enhance early strength development and reactivity, particularly when the SiO_2/Al_2O_3 and SiO_2/CaO ratios are optimized [31] [32].

Additional research on raw material blends has demonstrated that waste glass powder, RHA, and GGBS can improve GPC's compressive strength when used as a binder or fine aggregate [33]. Blends of FA and POFA-based geopolymers have also been found to perform better than those based on GGBS and SF [34]. Further studies on RuGPC using different source materials, such as MK, SF, RHA, and GGBS, with activator ratios $Na_2SiO_3/NaOH$ and Na_2O/SiO_2, and cured at an elevated temperature continue to explore ways to optimize mechanical properties and microstructure [13]. The integration of GGBS, SS, and CR in geopolymer concrete has not been extensively explored. However, this combination holds considerable promise for advancing the development of high-performance, sustainable building materials. The potential synergistic effects of these constituents could significantly enhance the physical and thermal properties of RuGPC, thereby expanding its applicability across structural and non-structural domains.

1.3. Effect of chemical compositions

Pursuing sustainable construction materials has intensified research into alternative binders and aggregates. GPC, a class of inorganic polymers, has gained significant attention as a viable substitute for traditional PC concrete due to its superior mechanical properties, environmental benefits, and durability. Synthesized through the alkali activation of aluminosilicate materials, geopolymers form a three-dimensional network of Si-O-Al bonds, significantly reducing carbon dioxide emissions associated with cement production [35]. This environmentally friendly process offers a promising solution for the construction industry. Incorporating waste materials, such as CR, from waste tires enhances the sustainability of geopolymers. CR has been explored as a partial replacement for conventional aggregates in concrete, addressing waste management issues while imparting properties like improved impact resistance and energy absorption [36]. However, optimizing the performance of RuGPC necessitates a thorough investigation of the chemical composition interactions.

Key chemical ratios, particularly those involving sodium (Na), silicon (Si), aluminum (Al), and sodium oxide (Na_2O), are crucial in determining GPC properties. The Si/Al ratio influences the formation of the geopolymeric gel, directly affecting mechanical strength and durability; a higher Si/Al ratio typically enhances mechanical properties. An optimal Na/Si ratio is essential for achieving desired workability and setting times [37–39]. Additionally, the Na/Al and H_2O/Na_2O ratios significantly influence the geopolymerization process, affecting the microstructure and performance of the concrete [40]. The alkali-activated materials' hardening mechanism relies on of dissolving Al, Si, and Ca from precursors, producing numerous cross-linked $Si-O-Si$, $Al-O-Al$, and $Al-O-Si$ bonds in tetrahedral coordination [41]. This process, comprising stages of nucleation, coagulation, and crystallization, leads to the formation of calcium aluminum silicate hydrates ($C-A-S-H$) and sodium aluminum silicate hydrates ($N-A-S-H$) depending on the precursor's chemical composition [42–44].

Research indicates that the Si/Al ratio directly correlates with the CS of geopolymer mortars, with a 10 % increase potentially enhancing strength by 20 %-40 % at three days [45]. In contrast, an increasing Na/Si ratio can reduce strength due to sodium carbonate formation (NaOH), which interrupts polymerization [45]. Low Si/Al systems yield primarily poly(sialate) structures, while high Si/Al systems form poly (sialate-siloxo) structures due to silicate species predominance [46] [33,47,48]. Elemental analysis has revealed distinct gel morphologies in hardened geopolymer specimens, highlighting the impact of chemical variations on geopolymer reactions and macrostructure. Variations in Si/Al, Na/Al, and Ca/Si ratios indicate the coexistence of calcium aluminum silicate hydrates (C-A-S-H) and sodium aluminum silicate hydrates (N-A-S-H), emphasizing the need to optimize chemical compositions for enhanced GPC performance [49] [50] [51].

Part et al. [30], found that CS from 13 to 42 MPa can be achieved with sodium silicate to sodium hydroxide ratios between 1.5 and 5.9, with the optimal ratio being 4.0, independent of RHA/FA hybridization ratios. They also noted that higher SiO_2/Al_2O_3 ratios reduced CS due to the high water uptake of RHA's cellular structure. The ideal curing conditions were established as a one-hour delay time, a 48-hour curing period, and a temperature of 60°C. The performance of RuGPC is influenced by several critical chemical compositions, including:

- Na/Si Ratio: Affects geopolymerization and the resultant strength and durability. A balanced Na/Si ratio is essential for a stable aluminosilicate network.
- Si/Al Ratio: Determines the structure and properties of the geopolymer binder, with higher ratios enhancing mechanical strength and chemical resistance [37,38].
- H_2O/Na_2O Ratio: This ratio impacts workability and setting time. Optimal water content is crucial for desired consistency and strength.
- Na/Al Ratio: Influences the degree of geopolymerization and the development of mechanical properties. Proper Na/Al ratios ensure sufficient alkalinity for effective polymerization.
- Grade of Rubber: Different grades of CR affect dispersion, bonding, and overall performance. Selecting the appropriate grade maximizes the benefits of rubber incorporation.

Despite extensive research on geopolymers and RuGPC, a significant gap remains in understanding the synergistic effects of these chemical compositions on RuGPC properties. Most studies have focused on individual impacts or independent addition of CR without a comprehensive analysis of their combined effects. Addressing this gap is essential for developing optimized mix designs that fully leverage both geopolymer technology and CR incorporation [52]. This study aims to fill this gap by providing a detailed analysis of the combined effects of key chemical compositions on RuGPC performance, contributing valuable insights for developing sustainable and high-performance construction materials. The literature highlights the potential of incorporating CR into geopolymer-based materials for construction. However, an increase in the percentage of rubber incorporation generally results in a reduction in material strength. This observation emphasizes the need for a comprehensive analysis to determine the optimal rubber content that balances performance enhancement and strength retention. Additionally, the size of the rubber particles remains a subject of debate, as it significantly impacts the material's overall performance. To address these critical questions and challenges, a systematic investigation is required. Moreover, the effects of varying chemical compositions, specifically the ratios of Na/Si, Si/Al, H_2O/Na_2O, and Na/Al, on the physical and thermal behavior of geopolymer concrete incorporated with crumb rubber particles remains undiscovered. This study aims to develop a predictive model to analyse the mechanical, thermal, and microstructural properties of RuGPC and understand the parameters that influence their performance the most using ML-based models. The model will examine the effects of both the quantity and size of CR in the mixture alongside other relevant parameters specific to SS-GGSS-based geopolymer chemical compositions.

1.4. Objectives of the Study

Despite numerous studies on CR-enhanced GPC, research on the effects of alkali activator ratios, such as Na_2SiO_3/NaOH, remains limited. Additionally, there is limited data on the effects of CR percentage and crusher dust (CD), curing temperatures, curing time, types of geopolymer source materials (SS and GGBS combined), and chemical compositions on the mechanical, thermal, and microstructural properties of RuGPC mortars and concrete. The lack of understanding of these parameters hinders the widespread use of RuGPC in the construction industry. Therefore, this study aims to investigate the effects of these parameters. The specific objectives of the study are as follows:

1. To investigate the effects of different molarity (NaOH) and alkali activator ratios.
2. To examine the influence of CR and CD percentages on GPC.
3. To investigate the effects of varying chemical compositions, specifically the ratios of Na/Si, Si/Al, H_2O/Na_2O, and Na/Al.
4. To analyze the combined effects of these parameters.
5. To develop predictive models that analyse the mechanical, thermal, and microstructural properties of RuGPC and understand the most influential parameters on their performance using ML-based models.
6. To evaluate the economic viability of RuGPC.
7. To identify the most influencing parameters.

By systematically analyzing these variables, the research seeks to provide a deeper understanding of the interactions between chemical compositions and waste material incorporation, ultimately contributing to developing more sustainable and high-performance construction materials.

2. Experimental methodology

The methodology involves selecting raw materials, designing mixes based on various variables, casting the materials, and conducting subsequent testing. The data obtained from these tests is used to develop a predictive model. This model facilitates informed decision-making by establishing relationships between variables and material properties, thereby aiding in optimizing construction material development processes.

2.1. Raw Materials

In this research, materials were carefully selected and sourced to develop geopolymer-based composites. SS, obtained from the Vizag Steel Plant in the Vishakhapatnam district, was characterized by its grey colour, a density of 2.89 g/cm^3, and particle sizes ranging from 300 μm to 10 μm (Fig. 2 illustrates the particle size analysis curve). Chemical analysis revealed significant components, including SiO_2 (36.9 %), Al_2O_3 (12.1 %), CaO (38.8 %), and MgO (7.69 %). Microscopic examination showed irregular particle morphology, which could influence mix workability.

GGBS, another key ingredient, was also sourced from the Vishakhapatnam Steel Plant. GGBS had a white-brown color and finer particles, smaller than 150 μm, with its particle size distribution shown in Fig. 2. Microscopic analysis indicated spherical particle morphology (see Fig. 3a-b), enhancing both reactivity and workability. The chemical composition of GGBS included SiO_2 (36.8 %), Al_2O_3 (16.5 %), CaO (35.1 %), and MgO (6.26 %), along with traces of Na_2O and K_2O. Fig. 3 displays the SEM images of SS and GGBS. The SS particles are irregular, angular, and have a rough texture. In contrast, the GGBS particles, while exhibiting similar morphology, appear sharp and flaky. The SEM image of SS was captured at 500x magnification, whereas the GGBS image was

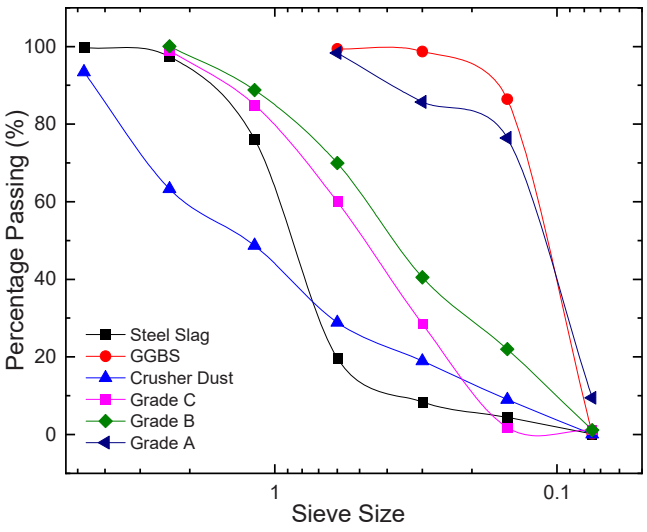

Fig. 2. Particle Size analysis of SS and GGBS.

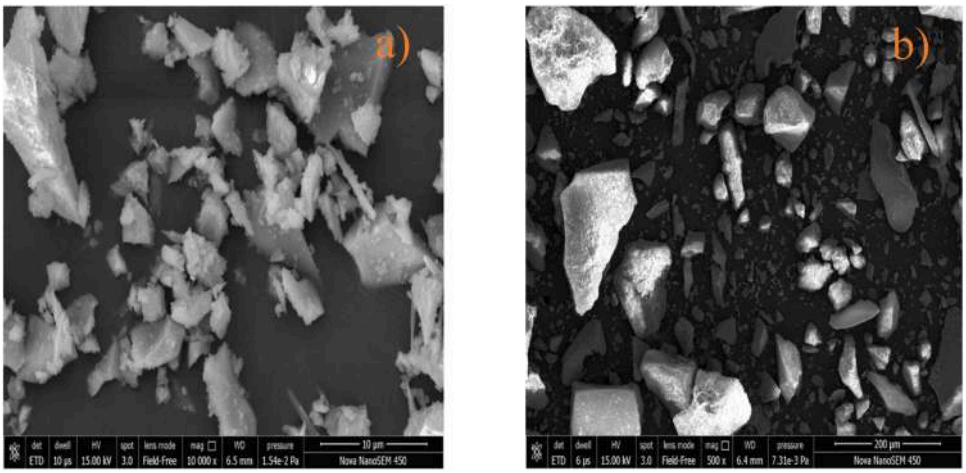

Fig. 3. SEM images at 20 μm of (a) GGBS (b) SS showing surface morphology.

taken at 10,000x magnification, demonstrating that SS particles are significantly coarser than those of GGBS. This variation in particle size can influence the reactivity of SS.

CD used in the study was sourced from quarries approximately 45 kilometres from the laboratory. Its particle size was limited to 2.36 millimetres, and the gradation curve is presented in Fig. 2. The density of the CD was 1891 kg/m^3. This material was considered inert, showing no reactivity in geopolymer formation but serving as a filler to enhance strength and stability.

Waste rubber, sourced from a discarded rubber factory in Vijayawada, was available in three grades: Grade A (particles passing through a 2-millimeter sieve), Grade B (particles passing a 0.841-millimeter sieve), and Grade C (particles passing a 0.595-millimeter sieve). These grades denoted as A, B, and C, respectively, have their particle sizes represented in Fig. 4.

We used a combination of alkali activators for the geopolymer formulation: sodium silicate (Na_2SiO_3) and sodium hydroxide (NaOH). These chemicals were procured from a local vendor, diluting the NaOH with water before use. In this study, four different sodium hydroxide molarity levels were experimented with (8 M, 10 M, 12 M, and 14 M). worth mentioning that molarity is a critical factor influencing geopolymer development and performance. The alkali solution was prepared using a specific ratio of 2.8 (Na_2SiO_3/NaOH).

3. Material development

This section details the mix designs and geopolymer preparation methods used in this research as illustrated in Fig. 5. The primary goal was to develop a predictive model, necessitating a substantial dataset from meticulously designed materials. Various variables were

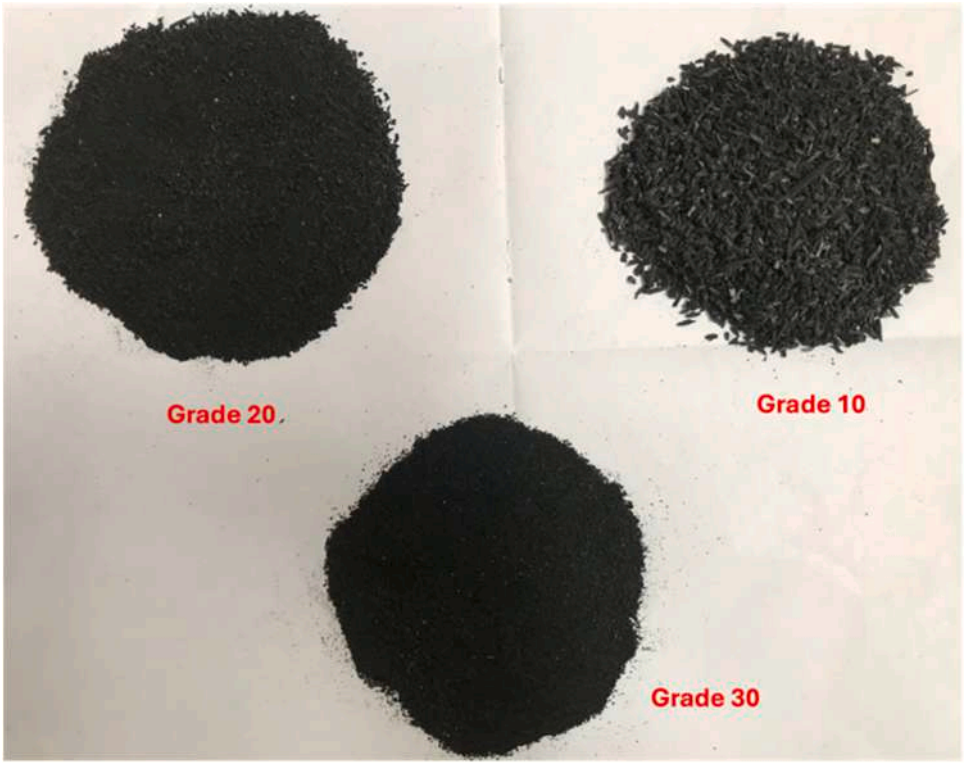

Fig. 4. Grades of CR used in this study.

Fig. 5. Flow process of RuGPC development [53].

considered, including the ratio of GGBS:SS, with three levels: 40:30, 35:35, and 40:30. Sodium hydroxide molarity had four levels: 8 M, 10 M, 12 M, and 14 M. CR grades included Grade A, Grade B, and Grade C, and the volume replacement of crumb rubber with CD was set at 10 %, 20 %, and 30 %. These factors resulted in 108 distinct mix combinations. Detailed mix designs are available in the manuscript's supplementary files (see Table A1 in Appendix A).

Fig. 5 illustrates the process of preparing crumb rubber-based geopolymer. Initially, all raw materials are carefully measured. A dry mixing phase follows, combining all solid ingredients in the specified proportions using a rotary mixer for 2–5 minutes. Next, the alkali solution is added, and wet mixing continues for 2–3 minutes until the mixture is homogeneous. The workability of each mix can vary based on the ingredient proportions, with a noted trend of decreasing workability as NaOH increases.

The mixture is then poured into moulds to cast RuGPC samples. After hardening, the samples are demoulded following a 24-hour curing period. To enhance reactivity, the blocks undergo an additional 24-hour curing in a heated oven at 60°C. Once removed from the moulds, the samples are cured again at 60°C. CS tests are conducted on the 28th days, and the resulting data is recorded for further analysis.

Adherence to relevant ASTM standards guided the execution of all tests during the experimental phase. To assess the integrity of hardened mortar, batches were cast in plastic moulds measuring 50 ×50 x 50 mm each. Maintained at a constant temperature of 22 ± 1°C, specimens remained in their molds for 24 hours before being immersed in water in the laboratory for 28 days. Mechanical properties were scrutinized through CS, density, and TC tests.

The TC of the rubberized geopolymer composite was determined using a hot-guarded plate apparatus. This involved positioning the RuGPC block between top and bottom plates, with the top plate heated to a specific temperature. Thermocouples placed at various points measured the heat transferred through the RuGPC block. TC (k) was calculated using Eq.(1):

$$q = -k \times a \times \frac{dt}{dx} \quad (1)$$

4. Experimental work discussion

This section illustrates the influence of various factors, including GGBS: SS, Ratio Molarity of NaOH, Grade of CR, Volume replacement of CR with CD, and other chemical compositions on the performance of RuGPC. Table 1 presents the effect of different levels of factors on the concrete's performance.

4.1. Compressive Strength (CS)

The experimentation involves analyzing four significant factors in the development of RuGPC. Each factor was examined at three levels, as detailed in the methodology section, allowing for a clear understanding of the influence of each parameter separately. The data revealed that increasing the proportion of SS in the mix results in a decrease in CS. Specifically, incorporating steel slag at 30 %, 35 %, and 40 % resulted in CS of 43.16 MPa, 40.38 MPa, and 38.96 MPa, respectively. SS and GGBS combine with an alkali solution to form a complex tetrahedral network of Si+ and Al+ ions. This network initiates the synthesis of an oligomeric gel, where the Si+ and Al+ ions saturate and dehydrate to form the geopolymer's three-dimensional structure. GGBS, being more reactive due to its morphology and chemical composition, increases strength with its higher content than SS.

Another parameter influencing the strength of the geopolymer is the molarity of the NaOH solution. Higher NaOH concentrations increase the Na/Si and Na/Al ratios, accelerating geopolymerization and promoting gel formation, thus enhancing material strength. The analysis showed a clear correlation between strength and NaOH molarity. As NaOH molarity increased, strength improved, with average CS of 38.91 MPa, 40.91 MPa, and 42.68 MPa for mixes with 8 M, 10 M, and 12 M NaOH, respectively. The highest CS of 56.67 MPa was achieved with 12 M NaOH, indicating its superior effectiveness.

The size of the CR, indicated by grade classification, also emerged as a crucial factor influencing the overall strength of the developed geopolymer. The average CS varied significantly across different grades of CR, highlighting the importance of particle size. CS were 33.75 MPa, 43.26 MPa, and 45.48 MPa for Grade A, Grade B, and Grade C rubber particles, respectively. Coarser Grade A rubber (passing through a 2 mm sieve) exhibited poor distribution within the matrix, leading to reduced strength. In contrast, finer Grade B and C rubber (passing through 0.841 mm and 0.595 mm sieves, respectively) demonstrated better distribution and stronger interlocking and bonding with the geopolymer binder, resulting in higher CS.

Finally, the percentage variation of crumb rubber within the

Table 1
Effect of three different levels of GGBS-SS ratio, Molarity of NaOH, Grade of CR, and Volume replacement of CR with CD on CS, Density, and TC.

Factors	Investigated factors' levels	28 days CS (MPa)			Density (kg/mm^3)			TC (W/mK)		
		Min.	Max.	Mean	Min.	Max.	Mean	Min.	Max.	Mean
GGBS:SS Ratio	R1 - (40:30)	28.87	54.63	43.16	1552	1850	1710.03	0.474	0.709	0.580
	R2 - (35:35)	27.28	51.48	40.38	1506	1795	1659.92	0.463	0.677	0.563
	R3 - (30:40)	26.21	49.14	38.96	1460	1740	1610.4	0.445	0.655	0.540
Molarity of NaOH	M1–8 M	25.40	50.77	37.65	1420	1678	1556	0.419	0.611	0.507
	M2–10 M	26.21	52.35	38.91	1460	1725	1599.67	0.445	0.649	0.5387
	M3–12 M	28.52	54.69	40.91	1520	1797	1665.81	0.471	0.685	0.568
	M4–14 M	28.85	56.57	42.68	1565	1850	1714.88	0.481	0.709	0.586
Grade of CR	C1 - Grade A	26.21	44.67	33.75	1460	1792	1622.85	0.445	0.709	0.560
	C2 - Grade B	31.89	54.63	43.26	1505	1815	1652.33	0.465	0.645	0.571
	C3 - Grade C	35.19	56.57	45.48	1545	1850	1705.185	0.472	0.675	0.582
Volume replacement of CR with CD	V1–10 %	36.79	56.67	47.22	1625	1850	1737.88	0.575	0.675	0.625
	V2–20 %	29.35	51.25	41.03	1610	1835	1722.55	0.555	0.651	0.603
	V3–30 %	26.21	42.92	34.26	1545	1760	1655.11	0.472	0.562	0.516

geopolymer mix was critical. Analysis showed CS of 47.22 MPa, 41.03 MPa, and 34.26 MPa for CR replacement levels of 10 %, 20 %, and 30 %, respectively. An inverse relationship exists between CS and CR content. As the proportion of rubber particles increases, the occupied volume grows, leading to a decrease in strength and rigidity. This decrease is due to the disruptive influence of the rubber particles on the matrix's structural integrity, making higher percentages of CR unsuitable for commercial applications due to significantly compromised material strength.

Figs. 6a-c and 7a-d delve into the CS of RuGPC with varying chemical compositions and molarity concentrations. Fig. 6a-c highlights the effects of Na/Si, H_2O/Na_2O, and Na/Al ratios, illustrating that the CS significantly fluctuates with changes in these compositions. Specifically, an optimal balance of these ratios is crucial for enhancing the CS, as

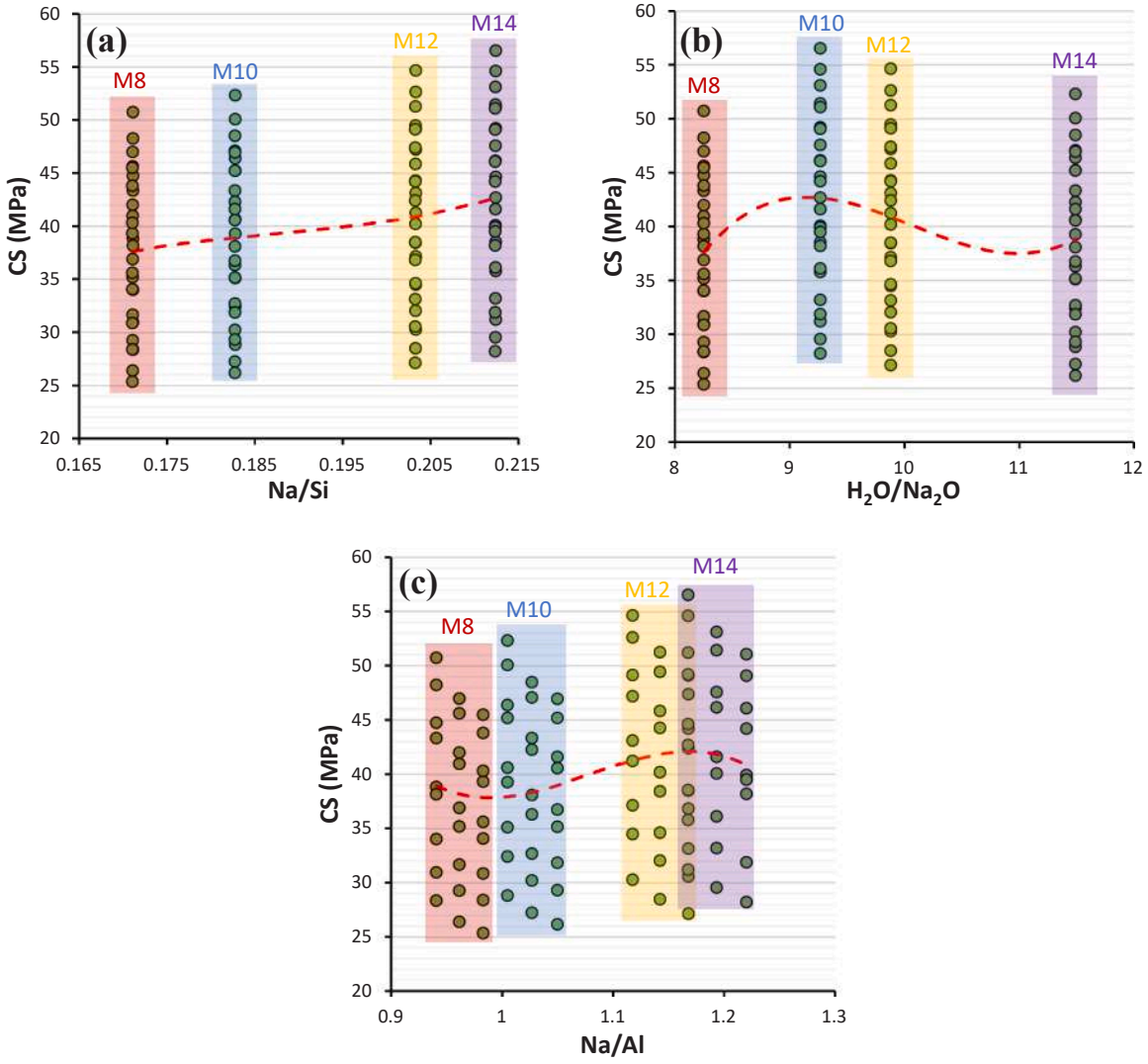

Fig. 6. Influence of chemical compositions on the CS of RuGPC foe different NaOH concentrations: (a) Na/Si, (b) H_2O/Na_2O, and (c) Na/Al.

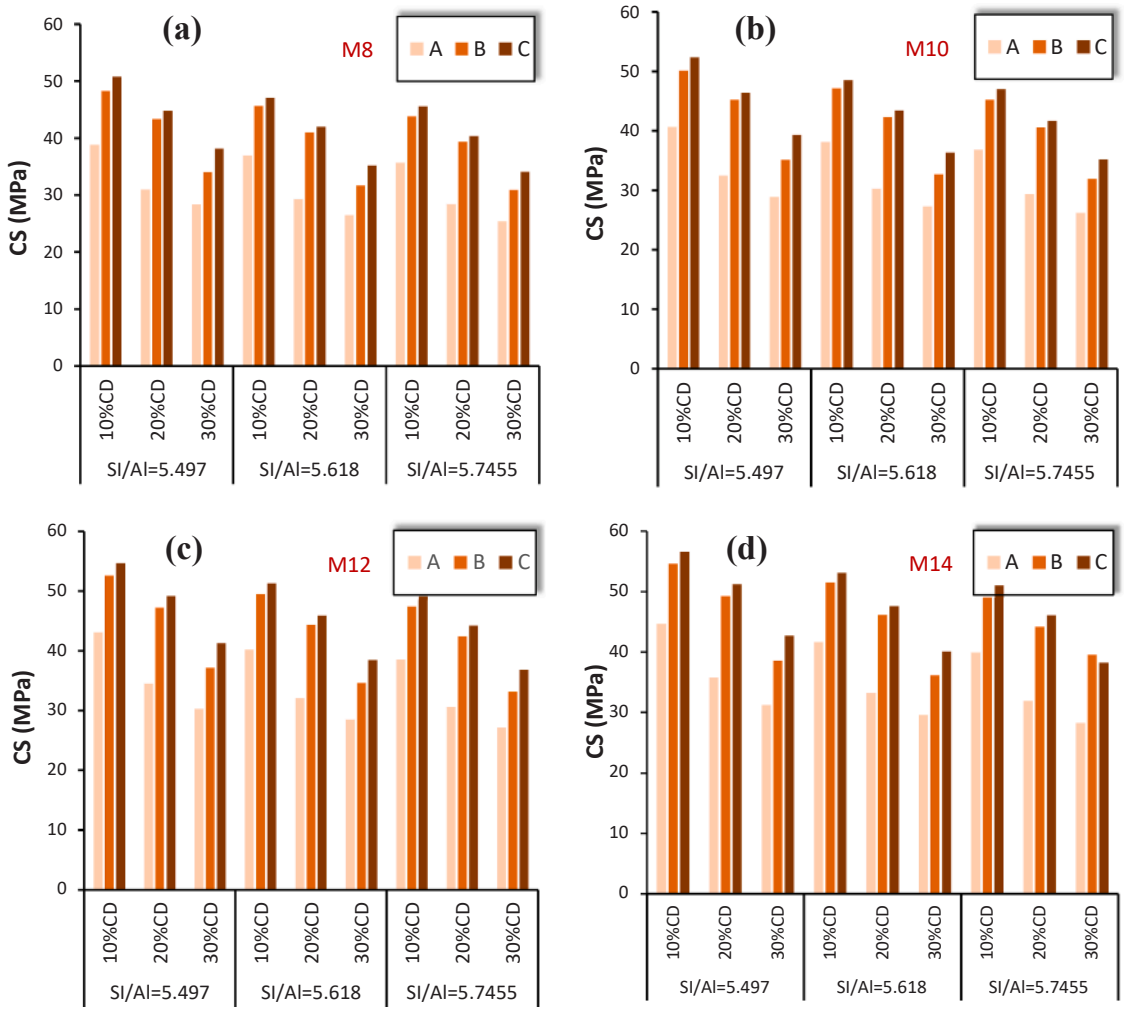

Fig. 7. Influence of Si/Al chemical compositions on the CS of RuGPC foe different NaOH concentrations: (a) M8, (b) M10, (c) M12, and (d) M14.

imbalances may lead to suboptimal mechanical performance. It is worth noting that any increase in CS was associated with an increase in Na/Si composition, which was endorsed by some works recently [54]. Fig. 7a-d expands on this by focusing on the Si/Al ratios at different molarities of NaOH (M8, M10, M12, and M14). The H_2O/Na_2O increases when the NaOH increases from M8 to M10; however, it decreases from M10 to M14. The CS of the samples systematically decreased as the molar Si/Al ratio increased, as reported in some recent works [55,56]. Conversely, a higher NaOH concentration resulted in a notable increase in CS. An increased Si/Al ratio in one-part geopolymer reduces the Si contribution to the final geopolymer product and a slower geopolymerization rate. This phenomenon is attributed to forming large, unreactive silicate oligomers rather than smaller, more reactive silicate species. This result aligns with the results reported by some researchers [57,58]. Moreover, results reveal that higher molarity concentrations generally bolster the CS, with M12 and M14 demonstrating superior performance for using 10 % grade (C) CR. The decreased CS in M8-M10 is associated with its lower Na/Si ratio and higher Si/Al ratio within the C–(N)–A–S–H type gel phases [59]. This suggests a pivotal role of Si/Al ratios in synergy with molarity concentration, indicating that precise adjustments in these parameters can lead to substantial improvements in RuGPC's mechanical robustness.

4.2. Bulk Density

The bulk density of building materials is a crucial consideration in the construction industry, as it influences the structural design of buildings. Lower bulk density is preferred, as it simplifies the construction process.This research has shown that incorporating CR reduced the bulk density of the geopolymer composites, a significant finding that could revolutionize the construction materials industry. CR's light and porous nature created a more porous structure, lowering the bulk density. The average bulk densities for geopolymer composites with 10 %, 20 %, and 30 % crumb rubber were 1737 kg/m^3, 1722 kg/m^3, and 1655 kg/m^3, respectively.

Furthermore, the size of the CR particles (referred to as the grade) also affected the density of the geopolymer composites. The average bulk densities for Grade (A), Grade (B), and Grade (C) CR were 1622 kg/m^3, 1652 kg/m^3, and 1705 kg/m^3, respectively. Finer CR particles are distributed more evenly throughout the matrix, resulting in better compaction during placement and slightly higher density values. Incorporating CR also increased the material's porosity. Both the quantity and the grade of CR significantly influenced these properties, underscoring the importance of considering these factors when designing and constructing buildings with RuGPC.

Figs. 8a-c and 9a-d examine the density variations of RuGPC concerning the same chemical compositions and molarity concentrations. Fig. 8a-c shows that the density of RuGPC is sensitive to the Na/Si, H_2O/Na_2O, and Na/Al ratios. A higher density is associated with specific combinations of these ratios, pointing to the importance of tailoring these compositions to achieve the desired density. When Na/Si is high, the density increases, aligning with Gholampour et al.'s results [60].

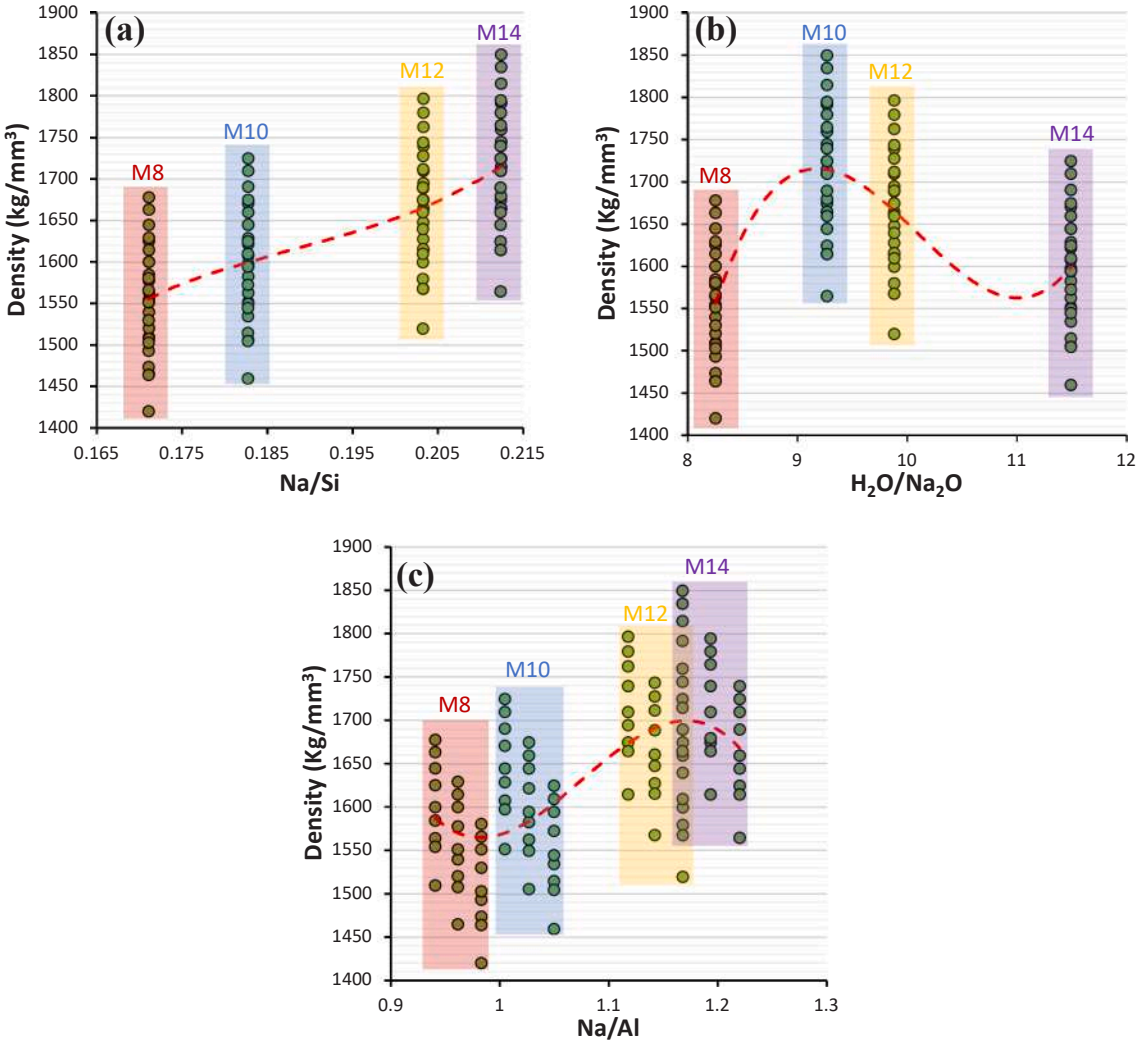

Fig. 8. Influence of chemical compositions on the density of RuGPC foe different NaOH concentrations: (a) Na/Si, (b) H_2O/Na_2O, and (c) Na/Al.

[61,62].

4.3. Thermal Conductivity (TC)

TC represents the heat flow through a material, is a crucial parameter that affects the insulation characteristics of building materials, and thus requires thorough analysis. The TC of the developed mixes was analyzed based on the factors listed in the table. The first factor is the ratio of SS to GGBS. The data suggests that increasing the SS content leads to a decrease in thermal conductivity values. Specifically, the incorporation of 30 %, 35 %, and 40 % SS resulted in thermal conductivity values of 0.58 W/mK, 0.56 W/mK, and 0.54 W/mK, respectively. As discussed in the previous section, higher GGBS content leads to better reactivity, forming a denser matrix. This denser matrix facilitates faster heat propagation, resulting in higher TC values. Additionally, the molarity of the NaOH solution has a similar influence. Higher molarity leads to better reactivity due to increased dissolution of Si and Al ions, resulting in a denser matrix and higher heat flow rates. The results indicate that NaOH molarities of 10 M, 12 M, and 14 M resulted in TC values of 0.53 W/mK, 0.56 W/mK, and 0.58 W/mK, respectively.

The addition of CR significantly impacted the TC of the material. Geopolymer blocks with Grade (A), Grade (B), and Grade (C) CR had TC values of 0.56 W/mK, 0.57 W/mK, and 0.58 W/mK, respectively. As discussed earlier, finer particles distribute more evenly within the matrix and compact well, making the geopolymer blocks denser with fewer pores compared to coarser grades of CR. Therefore, TC values are relatively higher when Grade (C) is incorporated into the matrix compared to the finer grade (Grade A).

Another crucial factor affecting TC is the percentage incorporation of CR particles. Incorporating CR at 10 %, 20 %, and 30 % resulted in TC values of 0.62 W/mK, 0.60 W/mK, and 0.51 W/mK, respectively. CR has a low specific gravity (approximately 1.1–1.15) and is porous, providing adequate void spaces that restrict heat transfer. Hence, as the incorporation of CR increases, the packing density of the product decreases, forming more voids and resulting in lower TC values. Higher CR incorporation is beneficial for providing insulation and enhancing thermal comfort for building occupants.

Figs. 10a-c and 11a-d address the TC of RuGPC, showcasing its dependence on chemical compositions and molarity concentrations. Fig. 10a-c highlights that Na/Si, H_2O/Na_2O, and Na/Al ratios significantly impact the TC, with specific ratios leading to lower TC, which is beneficial for insulation purposes. Fig. 11a-d further investigates the influence of Si/Al ratios at different molarities of NaOH. Higher molarity concentrations, notably M12 and M14, are associated with increased TC. This relationship underscores the potential of RuGPC for energy-efficient applications, where lower TC is desirable. The increase of Na/Al led to a reduction in the TC.

The TC of geopolymers indicates good thermal insulation, with lower density correlating to lower TC [63]. However, the increase of Si/Al led to a reduction in TC. Using SS-GGBS significantly increased the Si

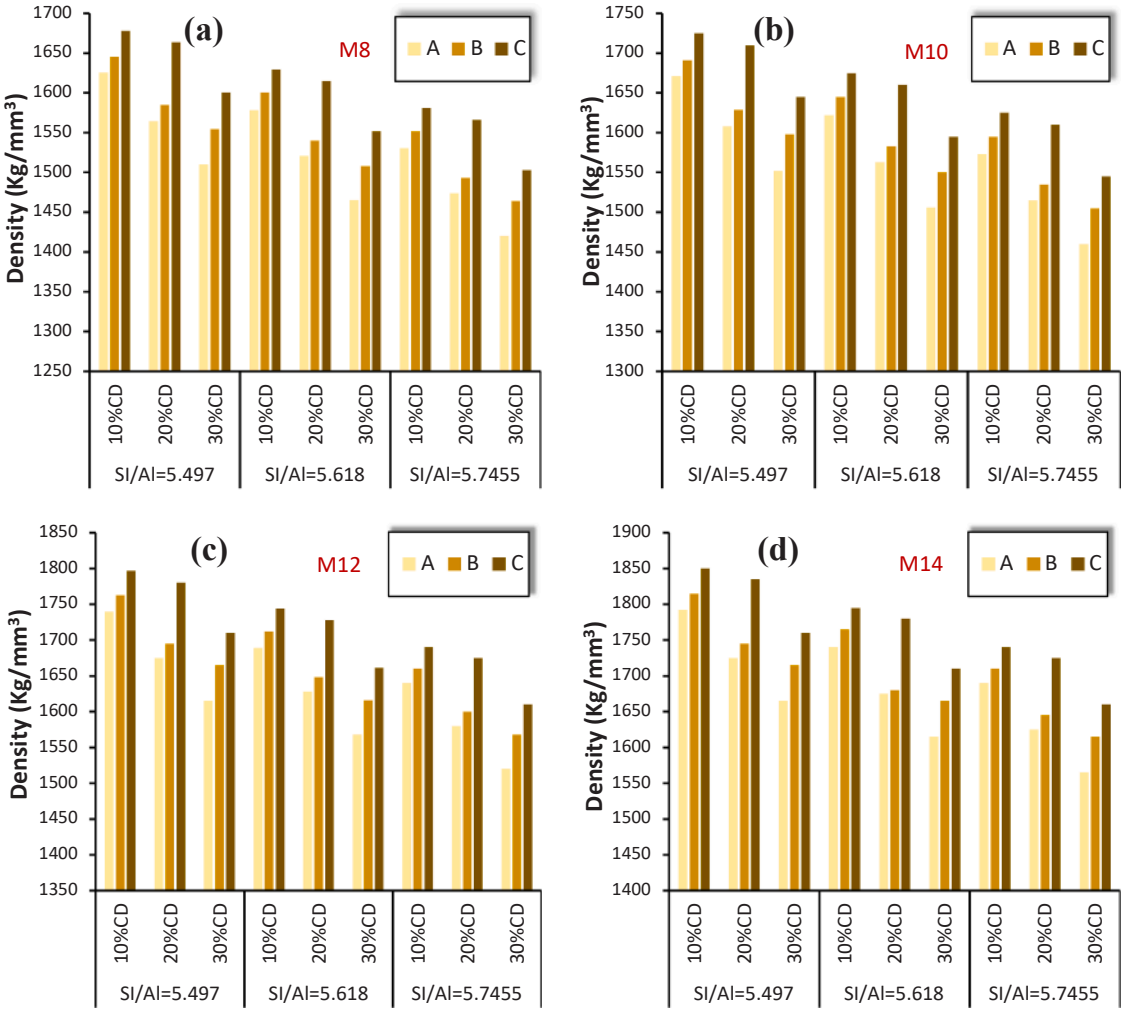

Fig. 9. Influence of Si/Al chemical compositions on the density of RuGPC foe different NaOH concentrations: (a) M8, (b) M10, (c) M12, and (d) M14.

content in the system, leading to higher Na/Si and Si/Al ratios. This resulted in a richer variety and greater content of gel phases [64].

The binder's porosity was reduced due to the filling capacity of these abundant gel phases, significantly enhancing thermal stability. Increasing the concentration of NaOH produced a higher TC and higher Si/Al ratios [61,62]. Moreover, results reveal that higher molarity concentrations generally higher the TC, with M8 demonstrating a lower value for 30 % grade (A) CR along with Si/Al=5.618 and M14 demonstrating the highest value for 10 % grade (C) CR along with Si/Al=5.497.

4.4. Micro-structural Analysis

4.4.1. Scanning Electron Microscopy analysis

The SEM analysis of steel slag and GGBS-based geopolymer composites gives us insights into their microstructure and elemental composition, showing the formation of key phases, unreacted particles, calcium hydroxide and geopolymer hybridization. The low-magnification (refer to Figure12(a)) SEM image shows a dense matrix with well-distributed particles, good compaction, and bonding within the geopolymer composite. At higher magnification (See Fig. 12(b)), the microstructure shows finer details, small unreacted particles of steel slag and GGBS, rubber, some microvoids, areas of incomplete reaction, or trapped air. These unreacted particles within the matrix are indicative of the raw materials' partial reaction, which can be further clarified by elemental mapping and EDS analysis.

Elemental mapping (Refer to Fig. 13a-b) shows a uniform distribution of key elements like Silicon (Si), Calcium (Ca), Aluminum (Al), and Iron (Fe), which are essential to understand the chemical interactions within the geopolymer matrix. The presence of Si and Al confirms the formation of aluminosilicate gels characteristic of geopolymer structures. The high amount of Ca from GGBS supports the formation of $C-A-S-H$ and $C-S-H$ phases, which are important for strength and durability. Moreover, the presence of calcium hydroxide ($Ca(OH)_2$) detected through the EDS spectrum indicates the incomplete reaction of GGBS, residual reactants that can affect the overall properties of the geopolymer.

The EDS spectrum analysis further confirms the elemental composition with major elements like Si, Ca, Al, Na, and Fe. The high amount of Si and Al indicates the formation of $N-A-S-H$ (sodium-aluminosilicate-hydrate) gels which contributes to the geopolymer structural integrity. The high Ca content supports the presence of C–A–S–H and C–S–H phases which enhance the composite mechanical properties. The presence of Na from the alkaline activator helps in forming the N–A–S–H gel and Fe from SS contributes to the material density. The formulation of these compounds is in alignment with XRD analysis; the presence of broad peaks corresponding to C–A–S–H and C–S–H phases and distinct peaks for calcium hydroxide indicates geopolymer hybridization. This hybridization forms a complex interlinked network of N–A–S–H, C–A–S–H, and C–S–H phases, which enhances the mechanical properties and durability of the composite. At an activator dosage of 2.8 (Na_2SiO_3/NaOH), the

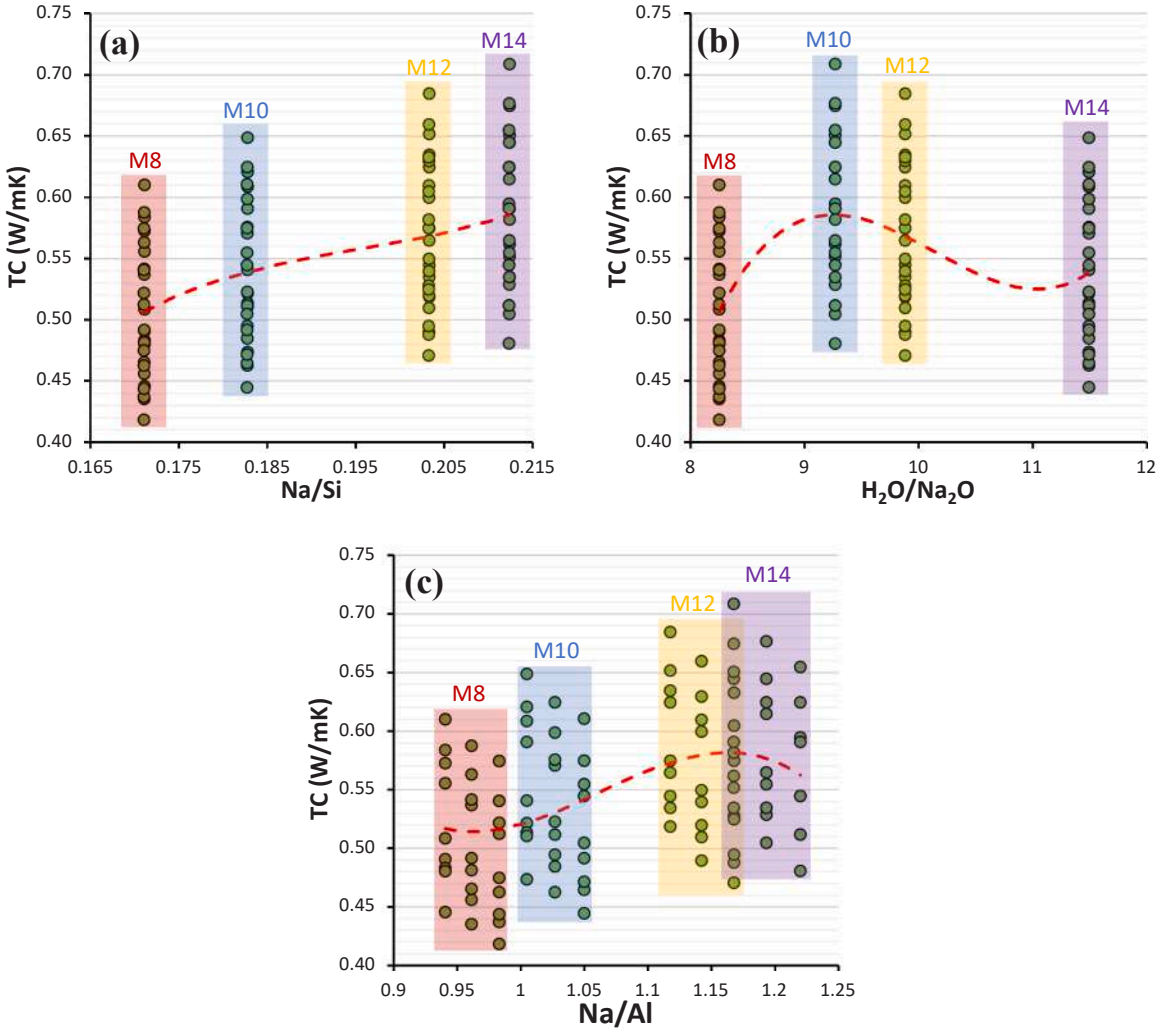

Fig. 10. Influence of chemical compositions on the TC of RuGPC foe different NaOH concentrations: (a) Na/Si, (b) H_2O/Na_2O, and (c) Na/Al.

microstructure of M14 was smoother, more intermixed, and denser compared to other concentrations, owing to its higher Na/Si ratio of 0.2123, which aligns with similar results of other works [65].

The detection of unreacted particles matches with the crystalline peaks in the XRD pattern, residual raw materials. SEM analysis, along with elemental mapping and EDS spectrum, gives us a comprehensive understanding of the microstructure and elemental composition of the SS-GGBS-based geopolymer composites.

Comparing the Na/Si, H_2O/Na_2O, and Na/Al ratios of the RuGPC mix, the M14-concentration mix exhibited higher Na/Si and H_2O/Na_2O ratios. This suggests that the reaction products were predominantly sodium–aluminosilicate hydrate rather than typical alkali-silica reaction gel or calcium–silicate hydrate. Incorporating SS-GGBS increased the Al/Si ratio and decreased the Na/Si ratio, with a slower reduction in the Na/Si ratio compared to Na/Al for other NaOH concentrations. This indicates that the formed gels were similar to calcium–aluminosilicate hydrate, reducing alkali-silica reaction expansion with higher SS-GGBS content.

In a 75 % waste glass powder (WGP) / 25 % GGBS-based AASG (alkali-activated GGBS-glass powder blended) paste, the Ca/Si, Si/Al, and Na/Si ratios (0.34, 8.78, and 0.27, respectively) indicate the formation of C–(N)–A–S–H gels as the main reaction products [59]. These gels effectively mitigate efflorescence, as reported by Wang et al. and Saludung et al. [66,67]. The blend's lower Na/Si and Ca/Si ratios and higher Si/Al ratio support efflorescence control. EDS analysis shows variations in atomic ratios due to reactive phases and the coexistence of *N–A–S–H and C–A–S–H* gels in SS-GGBS-based RuGPC, which increase Na/Si ratios. The slow release of Ca from GGBS initially forms N–A–S–H, which later converts into C–A–S–H (see Fig. 13a-b).

4.4.2. X-Ray diffraction analysis

The XRD analysis of SS and GGBS-based RuGPC, as shown in Fig. 14, shows a complex mixture of amorphous and crystalline phases, which are important for its mechanical properties. SS contains crystalline compounds like calcium carbonate (C) with peaks at 29.4° and 39.5° 2θ, quartz (Q) with peaks around 26.6° 2θ, akermanite (A) with peaks around 32.2° 2θ, dolomite (D) with peaks at 30.9° 2θ and larnite (L) with peaks around 32.5° and 41.4° 2θ. These compounds contribute to the material's inherent strength and durability: calcium carbonate and larnite contribute to density and mechanical stability, calcium carbonate and larnite contribute to density and mechanical stability; calcium carbonate and larnite contribute to density and mechanical stability, and quartz contributes to hardness and wear resistance. GGBS is amorphous with minor crystalline phases like calcium silicate hydrate (C–S–H, R with peaks at 29.4° and 32.2° 2θ, Q with peaks at 26.6° 2θ and calcium aluminum silicate hydrate (C–A–S–H,G) with peaks at 22.9° and 30.4° 2θ. These phases are important for the reactivity and binding of GGBS, C–S–H for early strength development, and C–A–S–H for long-term durability. When SS and GGBS are mixed to form the geopolymer composite, the resulting material has a hybrid structure with both amorphous and crystalline phases. The XRD pattern of SS-GGBS RuGPC shows the presence of several key phases: C with

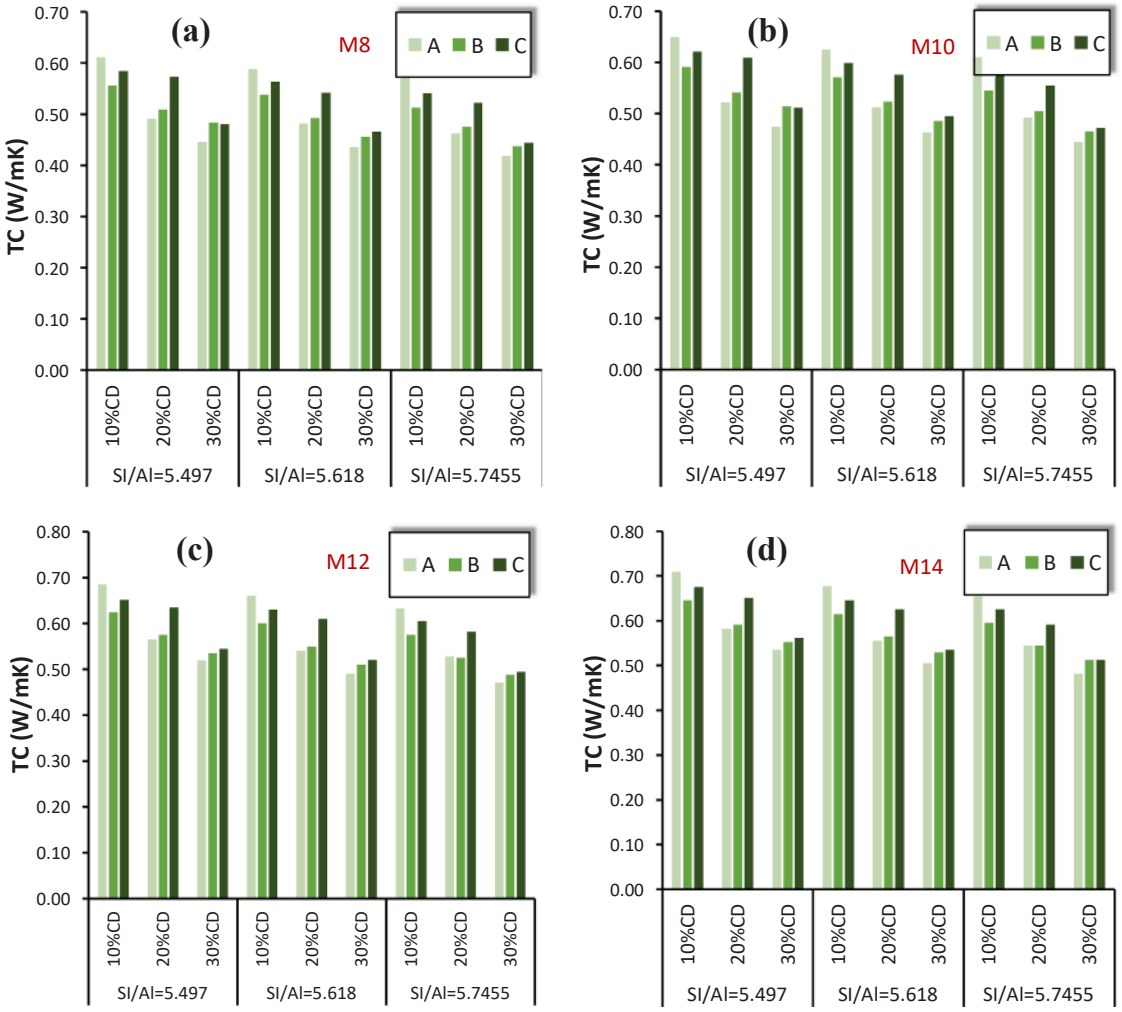

Fig. 11. Influence of Si/Al chemical compositions on the TC of RuGPC foe different NaOH concentrations: (a) M8, (b) M10, (c) M12, and (d) M14.

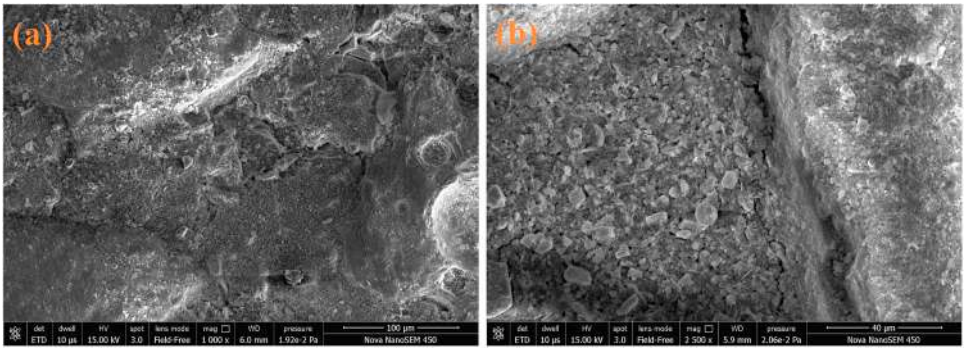

Fig. 12. FESEM image of binary blend of SS-GGBS-based RuGPC (a) Low magnification (b) High magnification.

peaks around 29.4° and 39.5° 2θ, Q with peaks around 26.6° 2θ, A with peaks around 32.2° 2θ, D with peaks at 30.9° 2θ, herschelite (N – A – S – H,S) indicated by the broad amorphous hump between 20°-35° 2θ, rosenhahnite (C – S – H, R) with peaks at 29.4° and 32.2° 2θ, gismondine (C – A – S – H,G) with peaks around 22.9° and 30.4° 2θ and L with peaks around 32.5° and 41.4° 2θ. The formation of herschelite (N –A –S –H gel) and rosenhahnite (C – S – H) in the geopolymer matrix is important. N –A –S –H gel indicated by the broad, amorphous hump in the XRD pattern is responsible for the composite's binding capacity, amorphous hump in the XRD pattern is responsible for the composite's binding capacity and flexural strength, toughness, and bending stress resistance.

C –S –H phases contribute to both early and long term contribute to both early and long term contribute to both early and long-term contributions to both early and long-term strength by providing a strong binding matrix. Gismondine (C – A – S – H) phases also contribute to long term contribute to the long-term durability and compressive strength so that the composite can withstand various environmental conditions over time.

The identified phases of typical reaction products, including

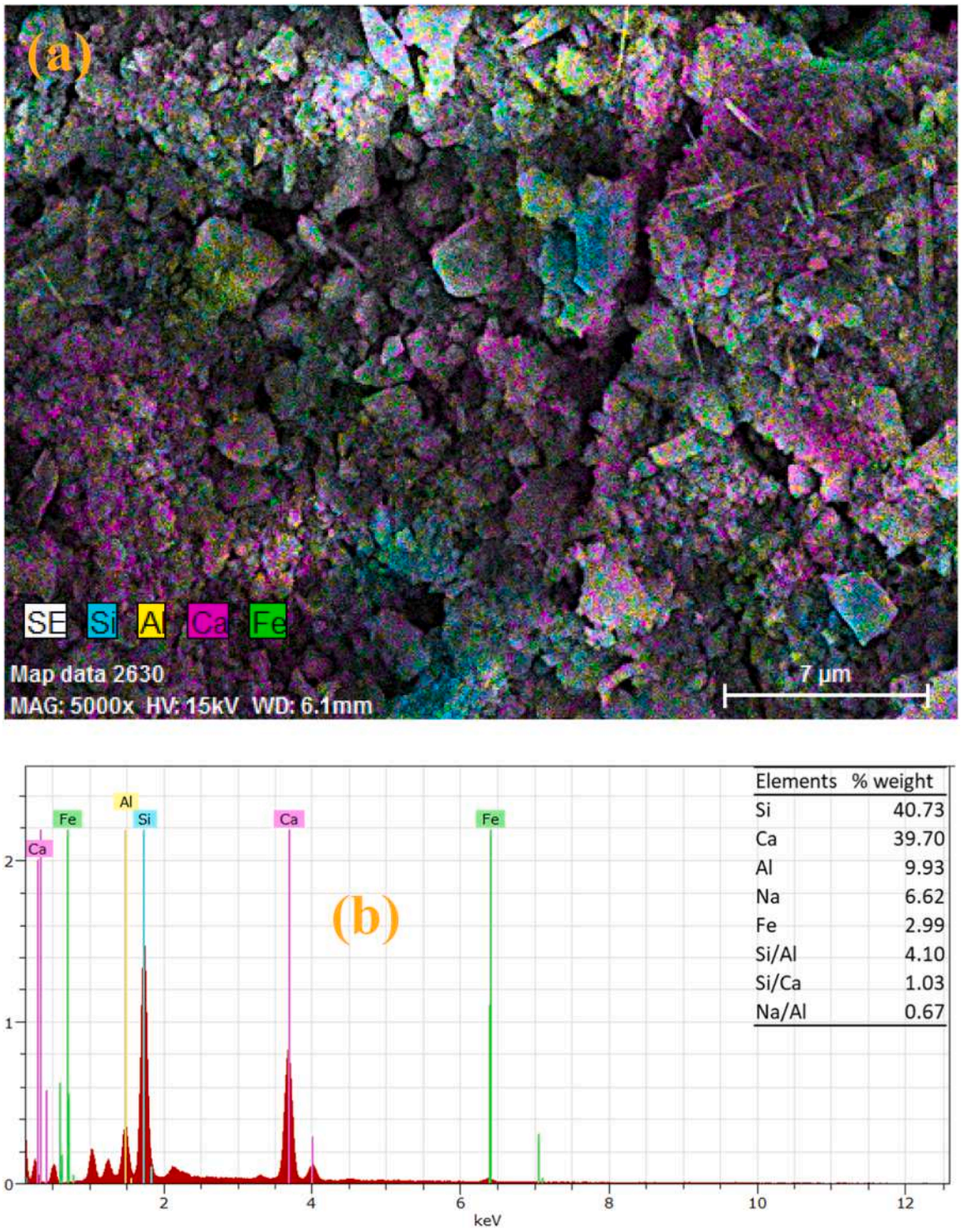

Fig. 13. (a) EDS image and mapping of a binary blend of SS-GGBS-based RuGPC (b) chemical elements.

C, C –S –H, and N –A –S –H gel, align with the findings reported by Puertas et al. [68]. In the alkali-activated SS-GGBS degraded zone, the Na/Si ratio ranged from 0.17 to 0.215. M14-concentration concrete samples exhibited the highest Na/Si ratios and showed no Na leaching, attributable to their lower alkali content compared to the alkali-activated SS-GGBS. This synergistic combination of phases due to the incorporation of both SS and GGBS gives the RuGPC its superior mechanical properties.

4.4.3. FTIR Analysis

The FTIR spectra, as shown in Fig. 15, show the characteristic peaks of SS, GGBS, and a geopolymer composite made from GGBS and SS. The SS spectrum features a broad peak around 3400 cm^{-1}, indicating O –H stretching vibrations from hydroxyl groups or absorbed water, and a sharp peak around 1630 cm^{-1}, attributed to the bending mode of H-O-H, confirming molecular water presence. Additionally, a peak around 1400 cm^{-1} suggests C-O stretching of carbonate species, while peaks around 870 cm^{-1} and 710 cm^{-1} correspond to Si –O –Si and Al –O –Si bending vibrations, typical in silicate materials. In the GGBS spectrum,

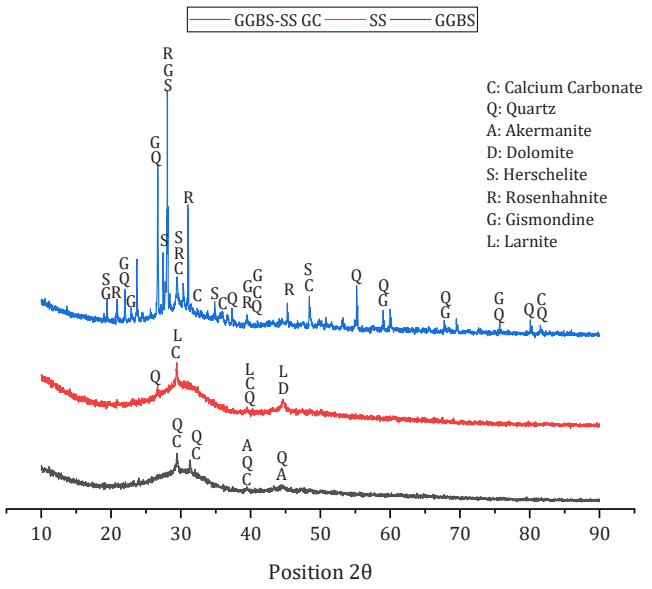

Fig. 14. XRD analysis of SS-GGBS-based RuGPC.

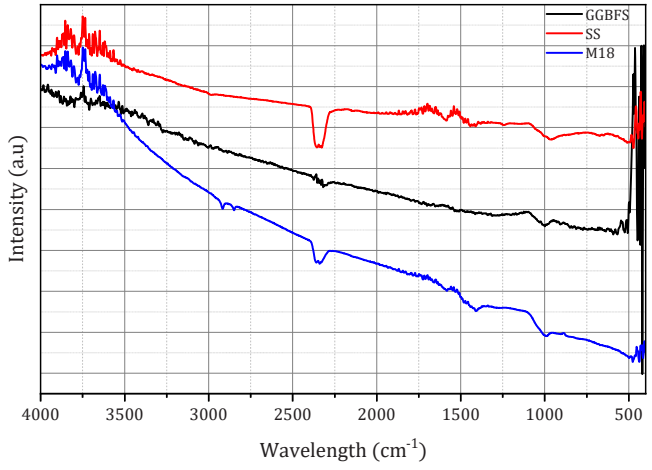

Fig. 15. FTIR analysis of raw material and SS-GGBS-based RuGPC.

the broad peak around 3400 cm^{-1} is again related to O-H stretching vibrations, and the sharp peak around 1630 cm^{-1} corresponds to the H –O –H bending mode. A broad peak around 1000–1100 cm^{-1}, indicative of Si-O-Si stretching vibrations, is prominent due to GGBS's high silica content, with a peak around 870 cm^{-1} associated with Al –O –Si bending vibrations and a weak peak around 450 cm^{-1} attributed to Si-O bending vibrations [69].

The SS-GGBS geopolymer composite spectrum displays similar broad peaks around 3400 cm^{-1} and 1630 cm^{-1}, indicating O –H stretching and H –O –H bending vibrations, respectively. The broad peak around 1000–1100 cm^{-1} is associated with Si –O –Si and Al –O –Si stretching vibrations, signifying the formation of the geopolymer network and quartz mineral [70,71]—peak around 870 cm^{-1} remains, representing Al –O –Si bending vibrations. These peaks and any new shifts or additional peaks suggest the formation of new phases or changes in the chemical environment due to geopolymerization. This result agreed with the previous literature [59,66,67]. Overall, the FTIR analysis reveals the chemical interactions and development of the geopolymer network in the composite material. This understanding is not only essential for determining its properties but also paves the way for potential applications, thereby demonstrating the significant impact of our research in the field of materials science and geopolymer technology.

5. Soft computing modelling

The models developed in this study aim to predict the properties of SS-GGBS-based-RuGPC, specifically targeting CS, density, and TC. The objective is to identify the best model that offers more accurate estimations than experimental methods. The dataset was divided into training and testing sets, comprising 76 and 32 datasets, respectively. Various models, including M5P-tree, random forest (RF), random tree (RT), linear regression (LR), support vector machine (SVM), and artificial neural network (ANN), were trained using the training datasets. For the ANN and SVM models, their weights and biases were optimized, while for the tree-based models (M5P-tree, RF, RT) and linear regression, their parameters and structure were adjusted during the training process to minimize prediction error. These models were then evaluated using the testing datasets. The performance of each model was assessed based on several criteria, including scientific accuracy, high correlation coefficient (CC) values, and low values of mean absolute error (MAE), root mean square error (RMSE), mean absolute percentage error (MAPE), and scatter index (SI).

5.1. M5P Tree

The M5P model tree, an extension of the M5P-tree algorithm, enhances conventional decision trees by incorporating linear regression functions at the leaf nodes [72]. This algorithm organizes data into a tree structure with root, internal, and leaf nodes connected by branches. Originally introduced by Quinlan [73], the M5P-tree is a powerful tool for regression analysis, assigning linear regression models to terminal nodes. By dividing the dataset into multiple sub-spaces, it applies a multivariate linear regression model to each. This approach effectively addresses continuous class problems and high-dimensional features, providing detailed insights into the nonlinear relationships within the data [74]. Node division criteria are based on error reduction, specifically the standard deviation of the class at each node. The attribute that maximizes error reduction is selected, initially creating a large, potentially overfitted tree. Pruning is then performed, replacing pruned subtrees with linear regression functions to enhance model efficiency. The M5P-tree model equation is similar to the linear regression equation, as shown in Eq.(2) and Fig. 16:

$$\begin{aligned}\text{Outcomes}(\text{CS}, \text{Density}, \text{and TC} = f_1(&\text{Na/Si}, \text{Si/Al}\\ &, \quad \text{H}_2\text{O/Na}_2\text{O}, \text{Na/Al}, \text{Grade of Rubber}\\ &, \text{and CR replacement percentage by volume of CD})\end{aligned} \tag{2}$$

5.2. Radom Forest (RF)

RF is a widely employed ML model renowned for its efficacy in both classification and regression tasks [76]. It operates as an ensemble method consisting of multiple unpruned classification or regression trees. The RF model's construction begins with the original training set $X = \{x_1, x_2, \ldots, x_n\}$ and corresponding labels $Y = \{y_1, y_2, \ldots, y_n\}$. From this original dataset, N new training sets $\{X_1, X_2, \ldots, X_N\}$ with labels $\{Y_1, Y_2, \ldots, Y_N\}$ are generated through random sampling with replacement, a technique known as bootstrapping. Each of these new training sets is then used to grow a decision tree $\{t_1, t_2, \ldots, t_N\}$, Where random features are selected at each node to determine the best split, thereby introducing variability and reducing overfitting [76]. Unlike traditional decision trees, RF trees are not pruned, which allows them to capture more complex patterns in the data. The final prediction of the RF model is obtained by aggregating the outputs of all individual trees using a majority voting rule for classification tasks or averaging for regression

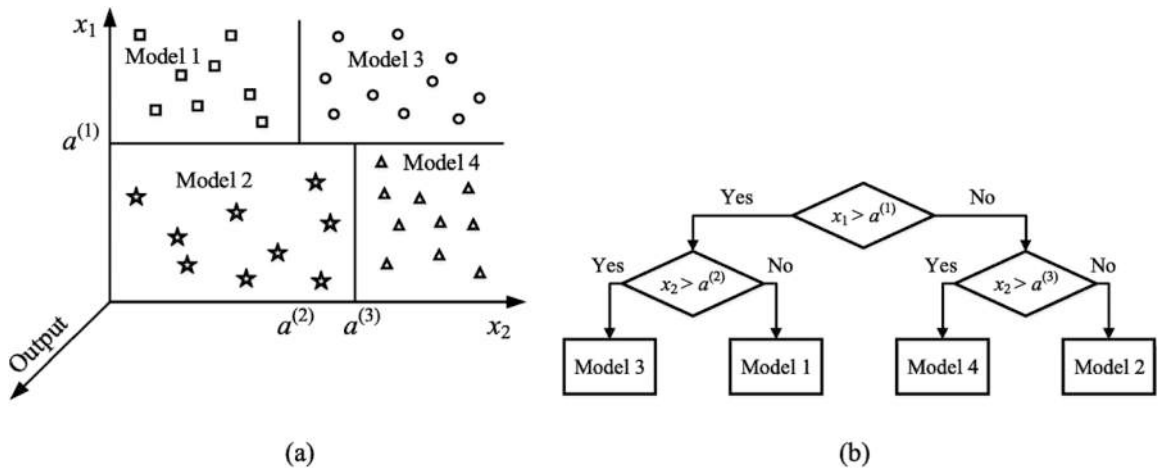

Fig. 16. Schematic of M5P: (a) input split; (b) model structure [75].

tasks. This aggregation process enhances the model's accuracy and robustness by mitigating the biases and variances associated with individual trees, leading to improved generalization on unseen data [77].

5.3. Radom Tree (RT)

Decision tree algorithms are highly effective due to their ability to provide human-readable rules for classification. In recent years, significant research has been conducted on random trees within machine learning. However, their application in the construction industry is still in its early stages [78]. Random trees, also referred to as regression-based decision tree algorithms, operate by considering K randomly selected attributes at each node during the tree-building process without any pruning [79–81]. A random tree is generated through a stochastic process, which is formed based on random selection and probabilities.

The methodology involves creating multiple trees where each tree T_i is built using a random subset of the training data. Randomness is introduced at each node to select a subset of features, which helps reduce overfitting and improve generalization [79]. Additionally, random trees can estimate class probabilities (or target means in regression cases) based on a hold-out set, a technique known as back-fitting [79,82]. Mathematically, if X is the original training set with n samples and labels Y, the algorithm can be described as follows: (i) Randomly sample the training set with replacement to generate N new training sets $\{X_1, X_2, \ldots, X_N\}$ with corresponding labels $\{Y_1, Y_2, \ldots, Y_N\}$. (ii) For each training set X_i, grow a decision tree T_i by:

- Randomly selecting K attributes at each node.
- Splitting the node based on the best attribute from the K selected.
- Continuing this process until the tree is fully grown without pruning.

The prediction for a new sample x can then be obtained by averaging the predictions from all trees (in the case of regression) or by using majority voting (in the case of classification) as shown in Eq.(3):

$$\widehat{y} = \frac{1}{N}\sum_{i=1}^{N} T_i(x) \tag{3}$$

This ensemble approach enhances the model's robustness and accuracy, making random trees a powerful tool in machine learning. They have promising potential applications in construction and other fields.

5.4. Linear Regression (LR)

LR is a statistical technique used to model the relationship between dependent variables (response variables) and independent variables (explanatory variables) [83,84]. The general formula for multiple regression models is (Eq.4):

$$Y = \beta_0 + \beta_1 X_1 + \beta_2 X_2 + \ldots.. + \beta_n X_n + \epsilon \tag{4}$$

In this equation, Y represents the dependent variable, β_0 is the intercept, β_j (where j=1,2,…,n) are the regression coefficients for each independent variable X_j, and $\epsilon\epsilon$ is the error term. Simple regression analysis involves only one independent variable, while multiple regression analysis includes two or more independent variables.

Several assumptions underpin linear regression models [83,84]:

- Existence: For any unique combination of independent variables X_1, X_2,…, X_j, the dependent variable Y is a random variable with a fixed average and variance within specific probability distributions.
- Independence: The observed values of Y are statistically independent and not correlated with each other.
- Linearity of Relationships: The expected value of Y is a linear function of the independent variables X_1, X_2,…, X_j. This means the relationship between Y and each X_j is linear.
- Homogeneity of Variance: The variance of the dependent variable Y remains constant across all levels of the independent variables X_1, X_2,…, X_j. This assumption is also known as homoscedasticity.
- Normality: The dependent variable Y follows a normal distribution for each combination of the independent variables X_1, X_2,…, X_j.

These assumptions are critical for the validity of the linear regression model, ensuring that the relationships observed in the data can be reliably generalized.

5.5. Support Victor Machine (SVM)

Support vector machine (SVM) is a widely utilized supervised machine learning algorithm, originally developed based on the principles of Vapnik-Chervonekis dimension minimization and structural risk minimization [85]. Known for separate effectively separating classes with a distinct margin, SVM is highly efficient in handling high-dimensional spaces with minimal memory usage. The primary objective of SVM is to identify the hyperplane that maximizes the margin for classifying samples. The hyperplane is defined by the following function [86] (Eq.5):

$$w^t x + b = 0 \tag{5}$$

X represents an n-dimensional vector, and w and b are the weight and bias, respectively. The optimization problem for determining this

hyperplane is formulated as a constrained problem (Eq.6):

$$s.t.\min_{w,b}\frac{1}{2}\|w\|\frac{1}{2}+C\sum_{a=1}^{l}L_a-y_a\left(\varnothing(x_a)^t w+b\right)\le L_a-1, L_a\ge 0, a=1\ldots,l \quad (6)$$

In this formulation, C is the penalty parameter, l is the number of training instances, L_a are the slack variables, and $\varnothing$ denotes the nonlinear mapping function. To determine the decision function for any test data, the following optimization problem is solved (Eq.7):

$$f(x)=sign(\sum_{a=1}^{l}\delta_a \quad y_a k(x, x_a)+b) \quad (7)$$

$where \delta_a \ge 0 \quad (a=1\ldots,l)$ are the Lagrange multipliers. This formulation ensures that the SVM can efficiently classify data by maximizing the margin between different classes, thus achieving high performance in various applications.

5.6. Artificial Neural Network (ANN)

ANN is a prominent technique in soft computing, known for its simplicity, high performance, and low computational cost [87]. Among the various types of ANN, the feed-forward neural network is the most commonly used and the simplest form [88]. This network type processes inputs on one side and delivers outputs on the other, utilizing unidirectional connections between neurons across different layers [89].

The feed-forward neural network includes two main types: the single-layer perceptron (SLP) and the multi-layer perceptron (MLP) [90, 91]. SLPs consist of only a single perceptron, whereas MLPs comprise several key elements: an input layer, hidden layer(s), activation functions, weights, an output layer, and neurons [92]. The input layer's role is to receive information from the external environment and pass it to the neurons in the hidden layer without any computation. Hidden layers between the input and output layers handle the bulk of the network's internal processing. The output layer presents the network's computations to the external world [93].

Adjacent layers in an MLP are fully interconnected through weights, and the activation function determines how neurons process input values to generate output values for the next layer [93]. A schematic diagram of a 3-layer MLP featuring 2 inputs, a hidden layer with 3 neurons, and 2 output units is depicted in Fig. 17.

5.7. Methodology of ML modeling

5.7.1. Models training

Models are typically built by dividing the data set into set training and testing set. The ratio of the training set to the testing set is 70:30, which means that 70 % of the data is used to train the model, and the remaining 30 % is used to assess it. To ensure consistency in the data division, a single random seed was used so that all models were trained and tested on identical datasets. A trial-and-error tuning method was utilized to establish the models' parameters, structures, and functions during the training phase. In the current experiment, three outputs (CS, density, and TC) are predicted using ML techniques. Surprisingly, while the forecasts for CS were successfully generated by all ML techniques. Using M5P, RF, RT, LR, SVM, and ANN models, estimates for restricted CS, density, and TC were made. Table 2 summarizes the ideal M5P, RF, RT, REPT, and SVM hyper-parameters and designs for the three outputs. In ANN, the learning rate (lr) hyperparameter is a crucial component of the optimizer function. According to the Keras documentation, the Stochastic Gradient Descent (SGD) optimizer employs a default lr scheduler that reduces the lr during the optimization process. This reduction follows a specific formula throughout the SGD algorithm (Eq.8):

$$lr=\frac{lr_o}{(1+decay\times epoch)} \quad (8)$$

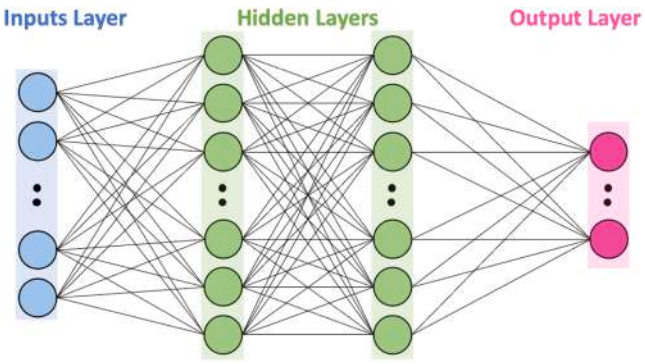

Fig. 17. ANN's general architecture [94].

5.7.2. Dataset

The predictive performance of a model is intricately tied to the diversity and quality of the data employed during its training phase. This study's dataset comprising 108 experimental observations was meticulously curated, encompassing input variables deemed influential in shaping the anticipated outcomes, particularly within the realm of reliable ensemble models constructed through ML techniques. Notably, the dataset featured six input and two output variables, introducing novel parameters such as $Na/Si, Si/Al, H2O/Na2O, Na/Al,$ Grade of Rubber, and CR replacement percentage by volume of CD. These variables were carefully selected to predict three crucial output parameters: the CS at 28 days, density, and TC. A comprehensive statistical analysis of the dataset is presented in Table 3, shedding light on the distribution characteristics of the variables under consideration. Additionally, Fig. 18 elucidates the workflow adopted in the modeling part of the current study, offering a structured overview of the research methodology employed.

5.7.3. Data pre-processing

The database used to train and evaluate ML models in this study was derived from experimental work conducted as part of the research. It

Table 2
Optimized hyper-parameters of ensemble models.

	Hyper-parameters	Optimized Value
M5P	min Num Instances	4
	Pruning	Pruned and Unpruned trees
	Max depth	5
RF	num Execution Slots	1
	num Iterations	100
	num Features	0
	Out of Bag (OOB)	True
	Random seed	5
	Max depth	5
RT	min Num	1
	min Variance	0.001
	Seed	5
	Max depth	5
SVM	c	1
	Type of filter	Normalize training data
	Kernel	PUK, RBF, PK, and NPK
	num Iterations	10
	Shrinkage	1
ANN	number of layers	Trial-and-error
	neurons per layer	Trial-and-error
	Random seed	5
	Initial learning rate (lr_o)	0.01
	decay	1e−6
	momentum	0.9
	Nesterovic momentum	True
	Epochs	250

Table 3
Detailed statistical analysis of input and output parameters used in the current study.

	Na/Si	Si/Al	H_2O/Na_2O	Na/Al	Grade of Rubber	RC replacement in % by Volume of CD	CS at 28 days	Density (Kg/mm^3)	TC (W/mK)
Mean	0.192	5.620	9.720	1.081	2.000	20.000	40.038	1634.176	0.550
Standard Error	0.002	0.010	0.114	0.009	0.079	0.789	0.748	8.731	0.006
Median	0.193	5.618	9.571	1.083	2.000	20.000	40.175	1628.500	0.545
Mode	0.171	5.497	8.248	0.940	1.000	10.000	45.240	1710.000	0.625
Standard Deviation	0.016	0.102	1.181	0.094	0.820	8.203	7.771	90.738	0.065
Sample Variance	0.000	0.010	1.394	0.009	0.673	67.290	60.395	8233.303	0.004
Kurtosis	−1.652	−1.514	−1.093	−1.512	−1.514	−1.514	−0.960	−0.434	−0.655
Skewness	−0.072	0.027	0.352	−0.046	0.000	0.000	0.011	0.080	0.217
Range	0.041	0.249	3.239	0.279	2.000	20.000	31.173	429.551	0.290
Minimum	0.171	5.497	8.248	0.940	1.000	10.000	25.397	1420.449	0.419
Maximum	0.212	5.746	11.488	1.220	3.000	30.000	56.570	1850.000	0.709
Sum	20.771	606.983	1049.725	116.738	216.000	2160.000	4324.076	176490.956	59.393
Count	108.000	108.000	108.000	108.000	108.000	108.000	108.000	108.000	108.000
Confidence Level (95.0 %)	0.0031	0.01946	0.22518	0.01796	0.15647	1.56476	1.48244	17.30863	0.01231

CR replacement in percentage by volume of CD

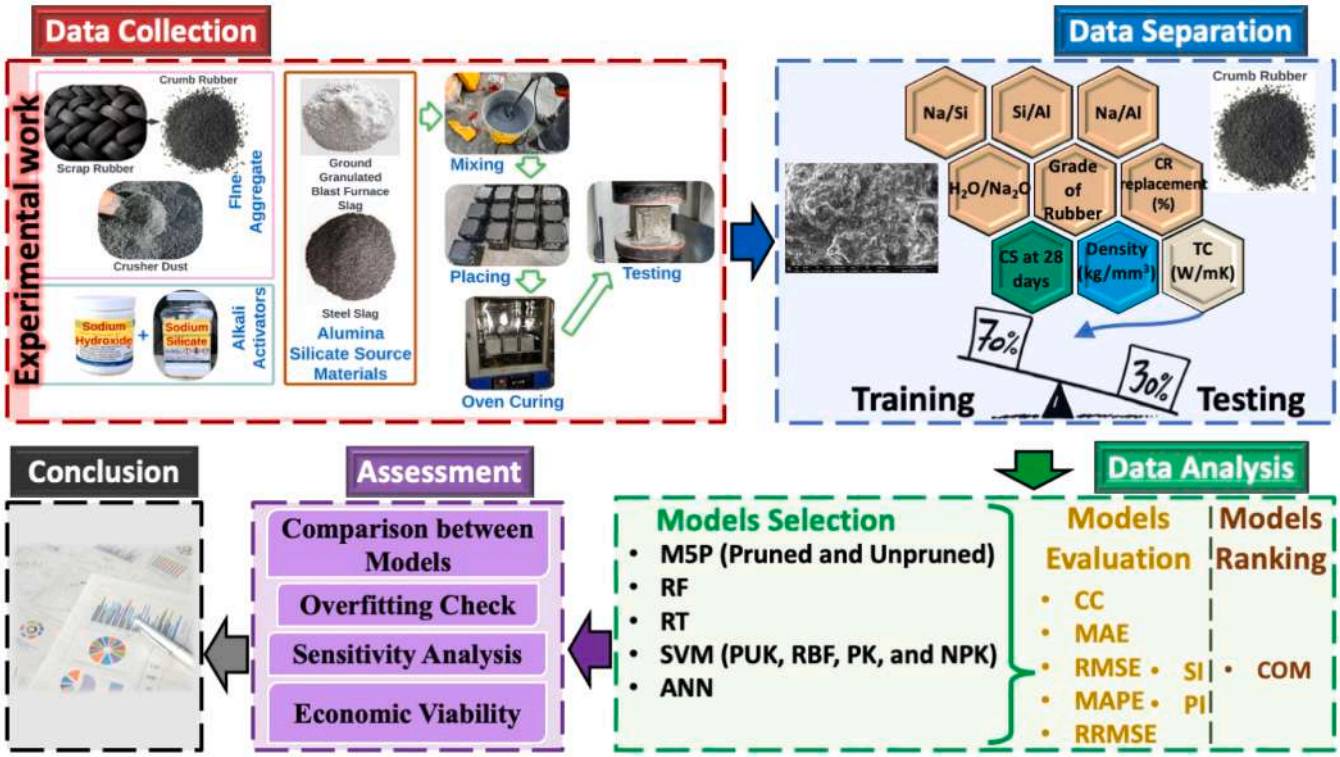

Fig. 18. Methodology adopted in the current study to predict outputs of RuGPC.

comprises six input variables and two output variables, encompassing 108 data instances, including new parameters: Na/Si, Si/Al, H_2O/Na_2O, Na/Al, Grade of Rubber, and CR replacement percentage by volume of CD. Moreover, Fig. 19 provides a visual representation of the Pearson correlation matrix, elucidating the interrelationships among the variables in the dataset. These visualizations offer valuable insights into the understanding of the data, aiding in the interpretation of model performance and predictive capabilities. To facilitate model training and evaluation, 70 % of the dataset was allocated for training purposes, while the remaining 30 % was reserved for testing the model's performance. Notably, the CS of blended cement concrete serves as the primary output parameter of interest.

5.7.4. Performance metrics

The models were trained using a substantial dataset of 68 entries, constituting 70 % of the data collected from current and prior studies. A separate test set of 29 entries was utilized to assess their performance, representing the remaining 30 % of the dataset [95–98]. The evaluation of these models involved a thorough analysis based on multiple criteria. Key factors included verifying the scientific accuracy of the model, ensuring minimal discrepancy between predicted and actual values, and achieving high correlation coefficients (CC) as indicated in Eq.(9) [99]. Additionally, the models were assessed on their ability to maintain low values across several performance metrics, including mean absolute error (MAE), root mean square error (RMSE), mean absolute percentage error (MAPE), scatter index (SI), comprehensive measurement (COM), relative RMSE (RRMSE%), and performance index (PI), as detailed in Eqs.(10−16). Additionally, to detect any potential overfitting, the objective function (OBF) indicator was applied, as described in Eq.(17). These criteria collectively ensured a robust evaluation of the models' predictive accuracy and reliability. The equations used to evaluate these metrics are given in Table 4.

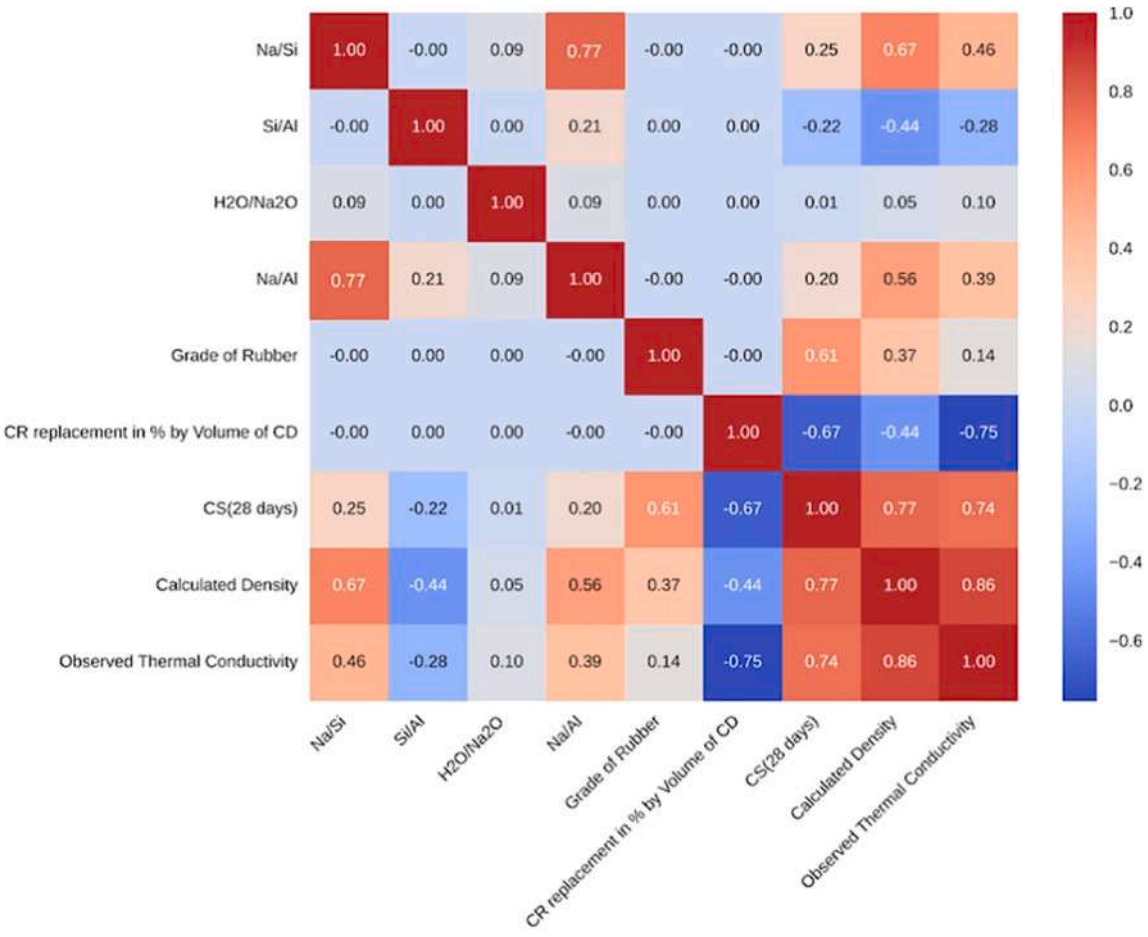

Fig. 19. Heat map for correlation between input and output parameters.

Table 4
Performance metrics equation [29–32].

Eq. No.	Parameter	Equation
9	CC	$CC = \frac{\sum_{i=1}^{N}(\mathrm{Pr}_i - \overline{\mathrm{Pr}})(Ac_i - \overline{Ac})}{\sqrt{\sum_{i=1}^{N}(\mathrm{Pr}_i - \overline{\mathrm{Pr}})^2 \sum_{i=1}^{N}(Ac_i - \overline{Ac})^2}}$ Where: Ac_i = observed value, Pr_i = predicted value, N = number of observations.
10	MAE	$MAE = \frac{1}{N}\sum_{i=1}^{N}\lvert \mathrm{Pr}_i - Ac_i \rvert$
11	MAPE	$MAPE = \frac{100}{N}\sum_{i=1}^{n}\frac{\lvert Ac_i - \mathrm{Pr}_i \rvert}{Ac_i}$
12	RMSE	$RMSE = \sqrt{\frac{1}{N}\sum_{i=1}^{N}(\mathrm{Pr}_i - Ac_i)^2}$
13	SI	$SI = \frac{RMSE}{\overline{S}}$ $\overline{S}$ = average observed value For excellent model (0.1)
14	COM	$COM = (\frac{1}{3} \times \frac{RMSE_{TRAINING} * MAPE_{TRAINING}}{CC_{TRAINING}}) + (\frac{2}{3} \times \frac{RMSE_{TESTING} * MAPE_{TESTING}}{CC_{TESTING}})$ The lowest is the best
15	RRMSE	$RRMSE = (\frac{RMSE}{\overline{S}}) \times 100$ For excellent model (0–10) %; good model (11–20) %
16	PI	$PI = \frac{RRMSE}{1 + CC}$ For good model (less than 0.2)
17	OBF	$OBF = (\frac{n_{TRAINING} - n_{TESTING}}{n_{TOTAL}})PI_{TRAINING} + (\frac{n_{TESTING}}{n_{TOTAL}})PI_{TESTING}$ For a good model (less than 0.2) For an excellent model (less than 0.1)

5.8. Results and discussion of ML modeling

Table 5 provides a comprehensive overview of the quantitative accuracy metrics, including CC, MAE, RMSE, MAPE, RRMSE, PI, and COM for each model across both training and testing stages. These metrics, illustrated in Fig. 20 (a-b), provide crucial insights into the models' performance and reliability in predicting concrete properties where CS prediction is shown in Fig. 20 (a1-b1), density prediction is shown in Fig. 20 (a2-b2), and TC prediction is shown in Fig. 20 (a3-b3),. The focus on testing set performance is justified by its importance in assessing model generalizability. A lower COM value reflects superior overall modeling proficiency, as detailed in Table 5.

5.8.1. Performance of M5P-based Models

This subsection evaluates the performance of the M5P-Pruned and M5P-Unpruned models in predicting CS, Density, and TC of concrete. The M5P model, which employs pruning techniques to enhance generalizability, was highly effective across all three properties. For The M5P-Pruned model achieved a high CC of 0.993 for CS during training, with low errors (MAE 0.696, RMSE 0.894, and RRMSE 2.266), maintaining similar performance during testing. For Density and TC, the model also showed strong performance with testing CC values of 0.987 and 0.977, respectively. The M5P-Unpruned model performed comparably well, with slightly lower errors for CS and similar results for Density and TC. Both models showed excellent generalization, making them reliable for predicting concrete properties. Key indices such as CC, MAE, RMSE, and RRMSE underscore their predictive proficiency (see Table 5), with the pruned model showing a slight superiority in generalization. The pruned model provided excellent generalization to new data, making it a

Table 5
Performance evaluating parameters of the models for 28 days CS, density, and TC of RuGPC.

	Training						Testing						COM	Ranking
	CC	MAE	RMSE	MAPE	RRMSE	PI	CC	MAE	RMSE	MAPE	RRMSE	PI		
CS														
M5P-Prund	0.993	0.696	0.894	0.049	2.266	0.011	0.993	0.740	0.945	0.235	2.183	0.011	0.164	2
M5P-Unprund	0.993	0.675	0.870	0.771	2.205	0.011	0.993	0.758	0.985	0.255	2.275	0.011	0.394	3
RF	0.998	0.587	0.714	0.508	1.810	0.009	0.982	1.709	2.081	0.729	4.809	0.024	1.152	7
RT	1.000	0.011	0.040	0.093	0.102	0.001	0.809	4.250	4.938	2.333	11.411	0.063	9.495	10
LR	0.985	1.073	1.309	1.183	3.318	0.017	0.988	1.011	1.261	0.469	2.913	0.015	0.923	5
SVM-PUK	1.000	0.029	0.033	0.099	0.083	0.000	0.977	1.750	2.121	0.694	4.901	0.025	1.006	7
SVM-RBF	0.981	1.400	1.844	1.053	4.675	0.024	0.981	1.624	2.085	0.466	4.818	0.024	1.319	8
SVM-PK	0.984	1.039	1.371	0.908	3.475	0.018	0.989	0.991	1.229	0.430	2.841	0.014	0.778	4
SVM-NPK	0.976	1.248	1.655	1.235	4.195	0.021	0.959	1.703	2.296	1.152	5.306	0.027	2.535	9
ANN	0.996	0.633	0.796	0.035	2.019	0.010	0.991	0.912	1.114	0.124	2.575	0.013	0.102	1
Density														
M5P-Prund	0.992	9.314	11.570	0.443	0.710	0.004	0.987	11.904	14.647	0.705	0.900	0.005	8.704	4
M5P-Unprund	0.995	7.643	9.525	0.327	0.585	0.003	0.988	10.929	14.815	0.596	0.910	0.005	7.003	3
RF	0.994	10.074	12.167	0.438	0.747	0.004	0.945	26.718	32.564	0.923	2.001	0.010	22.979	9
RT	1.000	0.267	0.774	0.012	0.048	0.000	0.853	44.536	48.054	1.192	2.952	0.016	44.789	10
LR	0.991	9.486	11.793	0.440	0.724	0.004	0.987	11.704	14.696	0.856	0.903	0.005	10.246	7
SVM-PUK	1.000	0.464	0.501	0.015	0.031	0.000	0.980	19.023	23.373	0.409	1.436	0.007	6.507	2
SVM-RBF	0.989	13.847	18.202	0.197	1.118	0.006	0.981	16.894	21.098	0.656	1.296	0.007	10.609	6
SVM-PK	0.992	9.081	11.785	0.660	0.724	0.004	0.986	12.175	15.194	0.597	0.934	0.005	8.750	5
SVM-NPK	0.979	13.630	18.342	0.509	1.126	0.006	0.979	14.750	18.575	0.639	1.141	0.006	11.263	8
ANN	0.999	4.103	5.049	0.024	0.310	0.002	0.999	4.469	5.383	0.055	0.331	0.002	0.238	1
TC														
M5P-Prund	0.981	0.010	0.012	1.450	2.239	0.011	0.977	0.012	0.015	1.991	2.546	0.013	0.026	3
M5P-Unprund	0.985	0.009	0.011	1.314	1.980	0.010	0.985	0.009	0.011	1.717	1.879	0.009	0.017	2
RF	0.995	0.007	0.008	0.974	1.554	0.008	0.950	0.020	0.026	2.295	4.478	0.023	0.044	5
RT	1.000	0.000	0.000	0.090	0.000	0.000	0.902	0.026	0.029	2.333	5.145	0.027	0.051	6
LR	0.956	0.015	0.018	1.783	3.367	0.017	0.930	0.021	0.025	2.856	4.337	0.022	0.062	7
SVM-PUK	1.000	0.000	0.000	0.092	0.056	0.000	0.947	0.021	0.027	2.219	4.794	0.025	0.043	4
SVM-RBF	0.942	0.017	0.025	1.967	4.681	0.024	0.907	0.023	0.036	2.298	6.234	0.033	0.078	10
SVM-PK	0.952	0.013	0.021	1.856	3.811	0.020	0.923	0.019	0.029	2.917	5.162	0.027	0.075	9
SVM-NPK	0.940	0.014	0.022	1.950	4.107	0.021	0.903	0.022	0.031	2.125	5.496	0.029	0.064	8
ANN	0.996	0.004	0.005	0.002	0.981	0.005	0.989	0.008	0.010	1.248	1.756	0.009	0.008	1

reliable choice for predictive modeling. Detailed numerical results and the weight of each model parameter is documented in Appendix A (Tables A3-A5), developed using the M5P tree model for both pruned and unpruned versions.

5.8.2. Performance of RF-based Models

The RF model displayed excellent training performance, with high correlation CC for CS (0.998), Density (0.994), and TC (0.995) alongside low errors. However, the testing phase revealed reduced generalization. For CS, the testing CC dropped to 0.982, with errors increasing significantly (MAE 1.709, RMSE 2.081, RRMSE 4.809). Similarly, for Density and TC, the testing CC values decreased to 0.945 and 0.950, respectively, with increased errors. This highlights the RF model's need for parameter fine-tuning to improve generalization while maintaining strong training accuracy. Key indicators show a disparity between training and testing phases, emphasizing a balance between model robustness and generalization.

5.8.3. Performance of RT-based Models

RT model achieved a perfect CC of 1.0 on the training dataset, indicating an exact fit for CS (see Fig. 20 (a1-b1)), Density (Fig. 20 (a2-b2)), and TC (Fig. 20 (a3-b3)) of RuGPC. However, its performance on the testing dataset was significantly poorer, with a CC of 0.809 and higher errors. This suggests severe overfitting, where the model learns the training data too well, including its noise and anomalies, but fails to generalize to new, unseen data. The RT model's sensitivity to overfitting highlights the necessity for techniques to enhance generalization. Pruning the tree to remove less significant branches or incorporating ensemble methods like Random Forests, which aggregate multiple trees to reduce variance and bias, can mitigate overfitting. Furthermore, ensuring the training data is comprehensive and representative of the entire data distribution. This finding underscores the importance of employing robust validation strategies, such as cross-validation, to ensure the model's reliability and performance on new data.

5.8.4. Performance of LR-based Models

LR, known for its simplicity and interpretability, demonstrated reasonable performance. For CS, the LR model achieved a strong CC of 0.985 during training, with low errors (see Table 5). However, the testing phase saw a slight decline in performance, with the CC dropping to 0.988. Similarly, the model performed well for Density, with a training CC of 0.991 and satisfactory testing results (CC of 0.987). When predicting TC, the model maintained good training accuracy (CC of 0.956) but showed reduced generalization during testing, with a CC of 0.930 and increased errors. Key indications include the LR model's solid baseline performance, particularly in predicting CS and Density, but the need for improvement in predicting TC and handling generalization issues. The study suggests that, while LR is useful, it may not fully capture complex relationships in the data, emphasizing the necessity of more advanced models for better predictions across all properties. The results emphasize the models can be used to predict the outcomes without for experimental testing (see Appendix A: Table A3-A5).

5.8.5. Performance of SVM-based Models

This subsection evaluates the performance of SVM models with various kernels (PUK, RBF, PK, and NPK) for predicting CS, Density, and TC of RuGPC. The SVM-PUK kernel demonstrated perfect training performance (CC of 1.0 for all properties) but struggled a bit with generalization during testing, where the CC dropped significantly for CS (0.977), Density (0.980), and TC (0.947) (see Table 5). The SVM-RBF model, while capturing non-linear patterns, showed moderate results with high training CCs (CS: 0.981, Density: 0.989, TC: 0.942), but experienced reduced accuracy in testing (CCs of 0.981, 0.981, and 0.907, respectively). The SVM-PK kernel provided the best overall

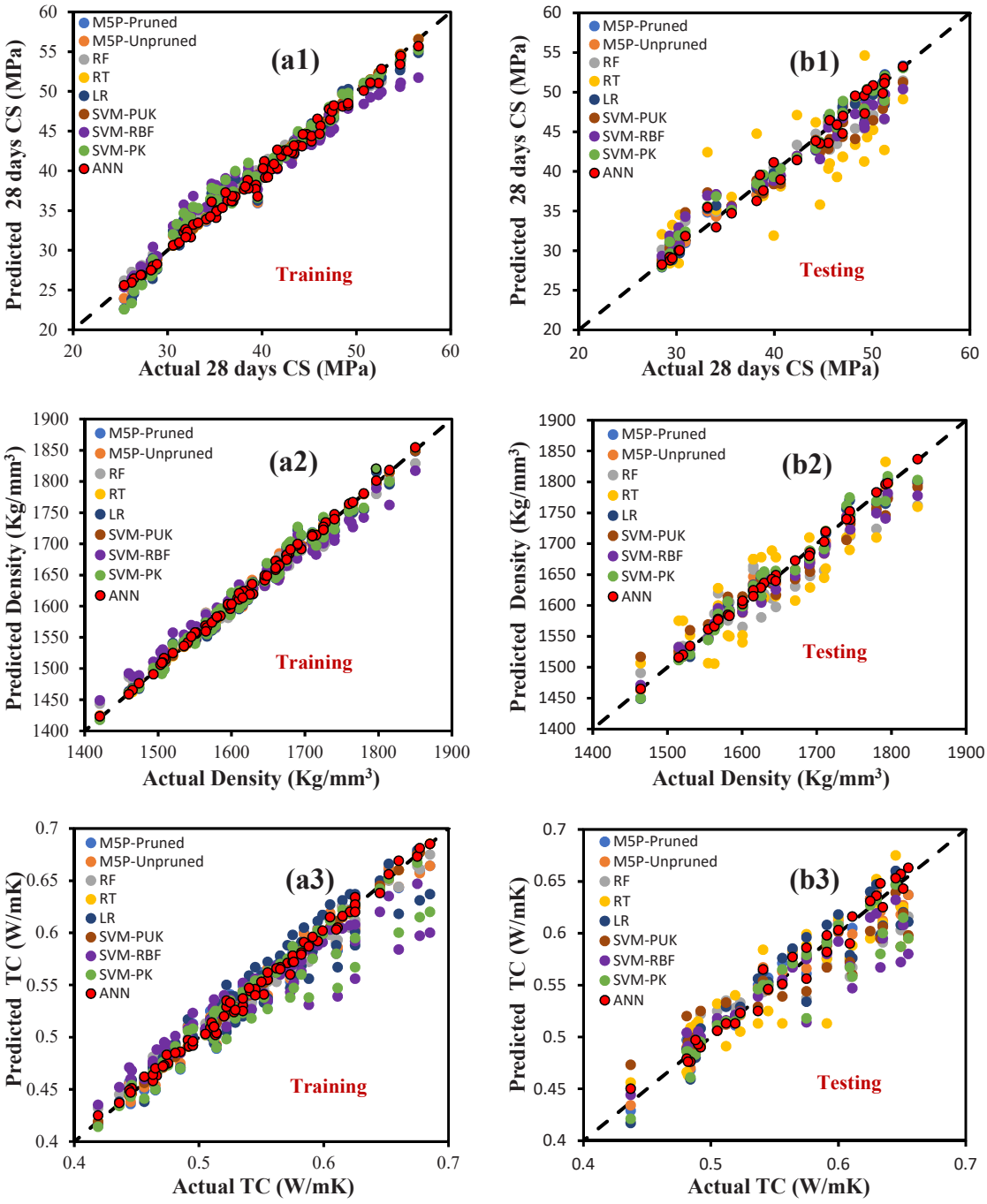

Fig. 20. ML-based model agreement for actual and predicted values: (a) training and (b) testing datasets.

balance, delivering high training CCs (CS: 0.984, Density: 0.992, TC: 0.952) and strong testing performance (CCs of 0.989, 0.986, and 0.923). Lastly, the SVM-NPK model offered good training results but lower testing accuracy, with CCs dropping to 0.959 for CS, 0.979 for Density, and 0.903 for TC. Key indications include the superior balance of the SVM-PK kernel between training and testing accuracy, making it the most effective for predicting concrete properties. The SVM-PUK kernel, despite its excellent training performance, requires improved generalization for new data. Both the SVM-RBF and SVM-NPK models would benefit from further hyperparameter tuning and validation to enhance predictive accuracy and performance. The results highlight the importance of kernel selection and model optimization when using SVM for complex datasets.

5.8.6. *Performance of ANN-based Models*

This study assessed the Artificial Neural Network's (ANN) performance in predicting Compressive Strength (CS), Density, and Thermal Conductivity (TC) of RuGPC, revealing strong results in both training and testing phases. For CS, the ANN achieved a high training CC of 0.996 and low training errors (MAE of 0.633, RMSE of 0.796, RRMSE of 2.019). Testing accuracy remained high, with a CC of 0.991 and minimal errors (MAE 0.912, RMSE 1.114, RRMSE 2.575). In predicting Density, the ANN showed excellent performance, with a training CC of 0.999 and testing CC of 0.999, alongside very low errors in both phases. For TC, the model also performed well, reaching a training CC of 0.996 and a testing CC of 0.989, indicating its strong ability to handle non-linear data patterns. Overall, the ANN model's high performance across all properties demonstrates its efficacy in learning from data and providing reliable

predictions, making it a valuable tool for RuGPC's property estimation.

5.8.7. Comparison of the applied ML-based models performance

This trend is further supported by the observations in Fig. 21(a-c), which highlight variations in the relative errors across different techniques. The results underscore the superior predictive capabilities of the ANN-based models, with an error margin of 1 %. Models utilizing M5P-Pruned and M5P-Unpruned techniques also performed well, showing an error margin of 1.5 % for evaluating CS, Density, and TC of RuGPC. Additionally, the SVM-PUK-based models demonstrated perfect prediction accuracy with an error margin of 5 %. In contrast, TR-based models exhibited the highest error margins at 10 %, 15 %, and 19 % for CS, Density, and TC of RuGPC, respectively, making them the least effective among the techniques applied.

Furthermore, the SI was calculated to evaluate the effectiveness of the predictive models [100]. As depicted in Fig. 22(a-c), all models demonstrated precise predictions for CS, Density, and TC of RuGPC. The ANN-based models exhibited particularly low SI values, indicating high accuracy: CS (0.022, 0.024), Density (0.003, 0.003), and TC (0.010, 0.018). The M5P-Unpruned model also performed well, achieving SI values of 0.020, 0.027 for CS, 0.006, 0.009 for Density, and 0.020, 0.019 for TC, although these were slightly higher than the ANN models. All models-maintained SI values below 10 %, underscoring their robust predictive capabilities.

Additionally, the CC/MAE ratio serves as a valuable metric for assessing the prediction accuracy of different models [101] used in RuGPC analysis. A higher CC/MAE ratio indicates better predictive capability. As depicted in Fig. 23(a-c), all models were evaluated based on this ratio. Notably, the ANN-based models demonstrated superior performance compared to the others, highlighting their effectiveness in enhancing prediction accuracy for RuGPC analysis. Furthermore, M5P-based models (both Pruned and Unpruned) also showed strong predictive capabilities.

5.8.8. Overfitting check

As shown in Table 9, all models had OBF values below 2 %,

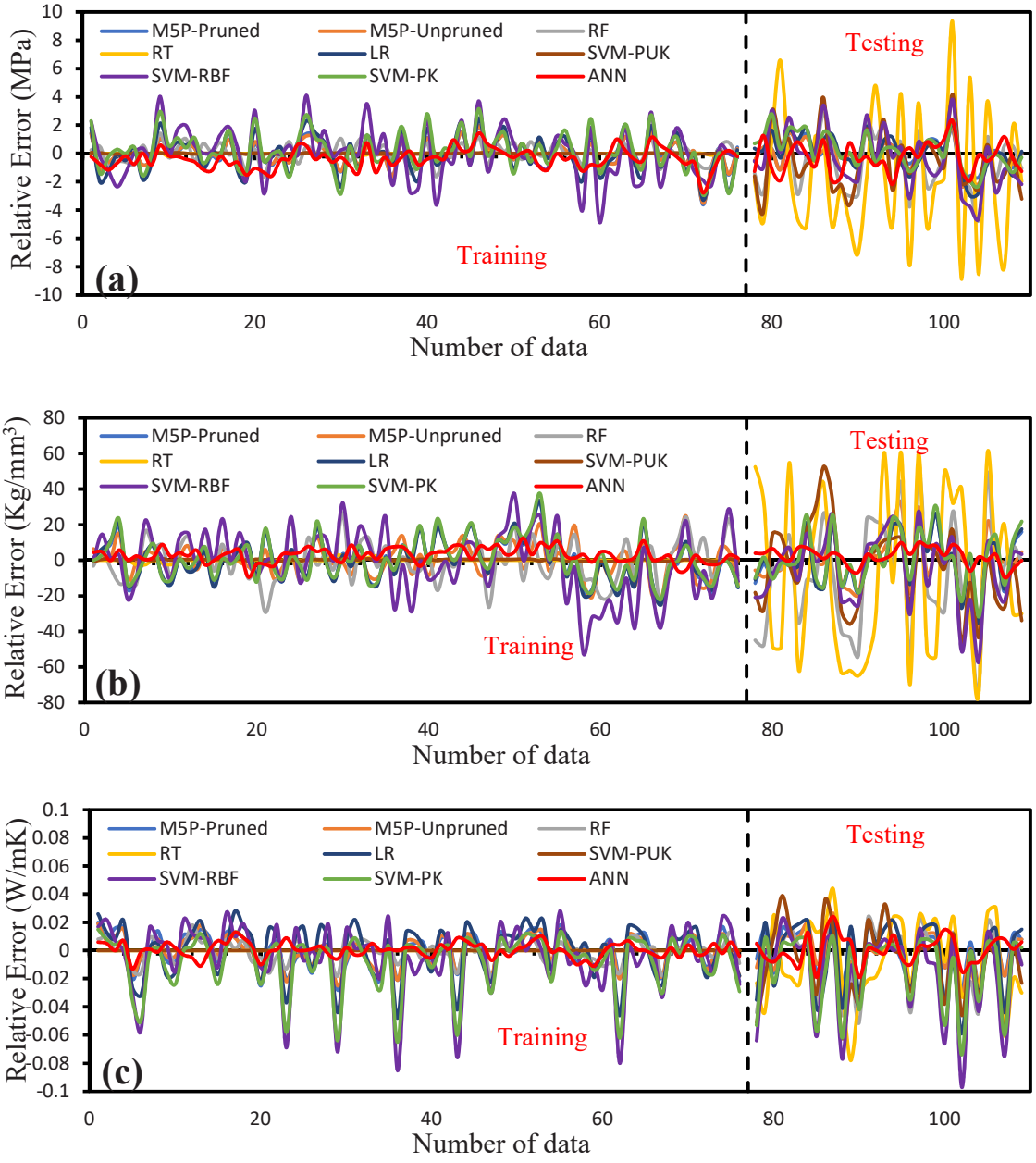

Fig. 21. Relative error of RuGPC's performance in training and testing stages: (a) CS, (b) density, and (c) TC.

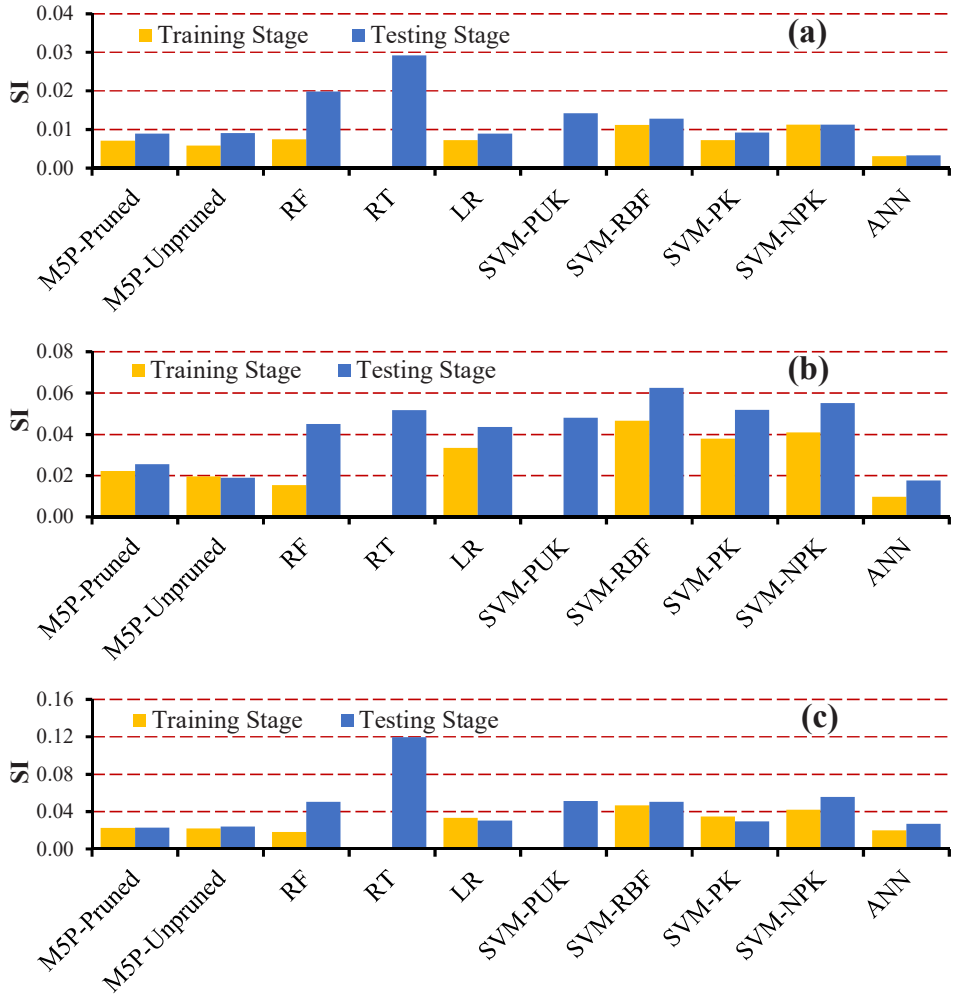

Fig. 22. Comparative SI plots of RuGPC's performance in training and testing stages: (a) CS, (b) density, and (c) TC.

demonstrating strong performance without signs of overfitting. This result highlights the robustness, reliability, and effectiveness of the models. The ANN models, in particular, showed the lowest OBF values, registering 0.007 for CS, 0.001 for density, and 0.004 for TC, further confirming their superior performance. Notably, all models maintained OBF values under 0.2 %, ensuring that overfitting was avoided during both the training and testing phases.(Table 6)

5.8.9. Sensitivity Analysis

Sensitivity analysis, as outlined by Verbeeck et al. [102], is a quantitative technique used in modeling and decision-making to evaluate the effect of variations in input parameters on a model's output. This method involves altering one variable at a time while keeping others constant, observing the resulting changes in the model's predictions. This analysis provides valuable insights into the model's robustness and reliability by quantifying its sensitivity to fluctuations in input parameters. As depicted in Fig. 24 (a-c) for the CS, Density, and TC of RuGPC, the outcomes reveal significant observations. Notably, the grade of rubber is shown to have a substantial influence on predicting CS, Density, and TC of RuGPC, underscoring its critical role in shaping the model's effectiveness. Additionally, the CR replacement percentage by volume of CD is identified as the second most influential parameter in determining CS.

6. Economic viability

The economic viability of using GPC is a crucial aspect to consider, especially in the construction industry where cost-effectiveness significantly influences material selection. In this study, the costs of RuGPC mixtures were calculated based on the constituent materials, excluding labor and transportation costs. The cost of RuGPC was 1.2–11.61 % lower than OPC concrete with maximum benefit obtained with 14 M Molarity and the lower was with 8 M Molarity as illustrated in Table 7. Such cost savings are critical, as they not only offer a more economical alternative but also align with sustainable construction goals by reducing carbon dioxide emissions. It is important to note that while some studies, such as Janardhanan et al., suggest that GPC may be slightly more expensive (by about 1.7 %) than OPC for grades up to 30 MPa, others like McLellan et al. have demonstrated that GPC can reduce both construction costs by 7 %, when fly ash is used [103]. Similarly, GPC could be 11 % less expensive than OPC, making it a more economically and environmentally favorable option. Despite findings indicating that GGBS-based GPC may cost around 7 % more than OPC, the overall reduction in environmental impact and the long-term savings through durability and isolation make it a viable choice [104,105]. Additionally, the economic index of RuGPC was calculated and compared with traditional concrete. The results endorsed that RuGPC showed slightly higher economic index than the traditional concrete with 10 M, 12 M, and 14 M (see Table A6 in Appendix A). On the other hand, the economic index was slightly lower than the traditional concrete with 8 M. It is worth mentioning that the economic index of the RuGPC was lower than that of OPC with low CR content. Therefore, while initial material costs for waste materials-based concrete may sometimes exceed traditional OPC concrete, the overall economic

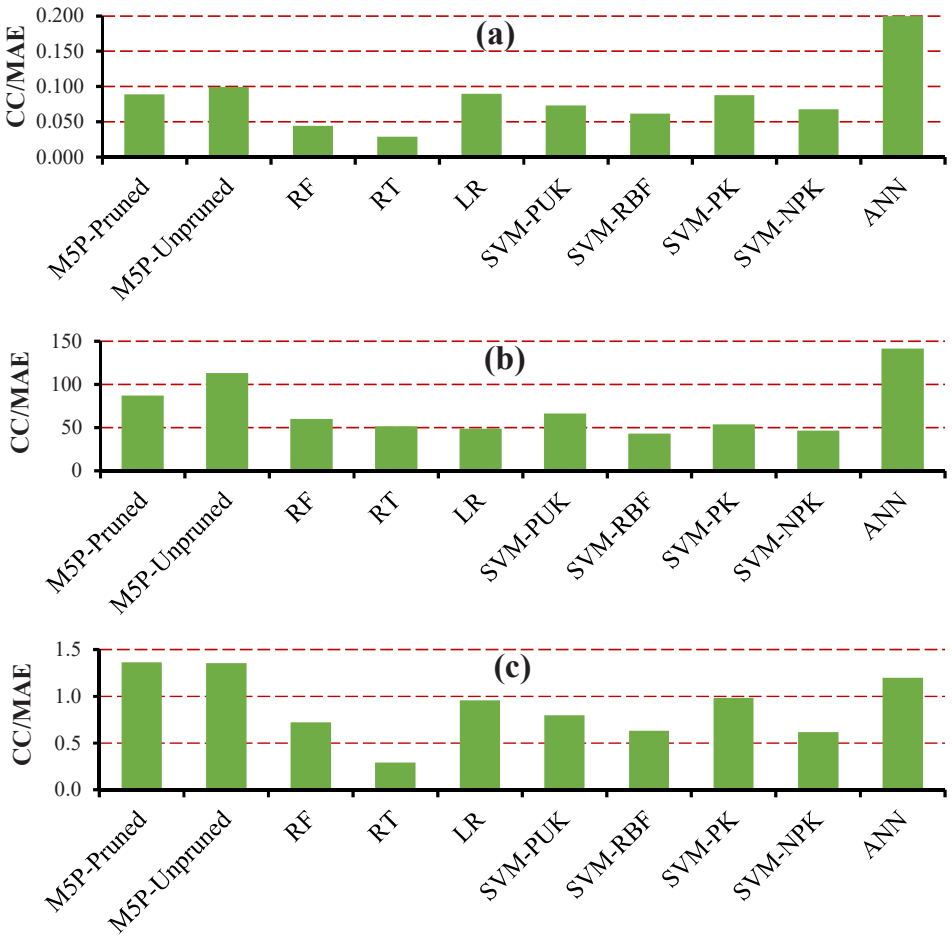

Fig. 23. CC/MAE ratio measured for all applied models: (a) CS, (b) density, and (c) TC.

Table 6
OBF values of predictive models.

Models	OBF of CS Models	OBF of Density Models	OBF of TC Models
M5P-Pruned	0.007	0.003	0.007
M5P-Unpruned	0.007	0.002	0.006
RF	0.010	0.004	0.009
RT	0.017	0.004	0.007
LR	0.010	0.003	0.012
SVM-PUK	0.007	0.002	0.007
SVM-RBF	0.015	0.004	0.018
SVM-PK	0.010	0.003	0.014
SVM-NPK	0.015	0.004	0.015
ANN	0.007	0.001	0.004

benefits derived from lower carbon footprint and potential savings, aligning with sustainable development goals (SDGs) [106,107]. The combination of economic benefits makes RuGPC a viable alternative to traditional concrete [108].

7. Conclusions

The primary objective of the research is to incorporate waste rubber for sustainable production of building materials. The research has successfully utilized the waste CR to develop a sustainable alternative, i.e., CR-based geopolymer. However, further, the focus was to analyze and develop a predictive model to analyze the behavior of critical factors playing a crucial role in the strength development of the material. In this quest, the research derived certain conclusions as follows:

- The study showed that RuGPC CS decreases with higher SS content—43.16 MPa at 30 % SS to 38.96 MPa at 40 % SS—and increases with NaOH molarity, reaching 56.67 MPa at 12 M. Finer CR grades increase strength (up to 45.48 MPa), while higher CR content reduces it to 34.26 MPa at 30 % CR and lowers bulk density (1655 kg/m^3 at 30 % CR). TC decreases with more SS (0.54 W/mK at 40 % SS) and higher CR content (0.51 W/mK at 30 % CR), but increases with NaOH molarity (0.58 W/mK at 14 M).
- The performance analysis of SS-GGBS-based RuGPC highlights the vital role of chemical compositions and molarity concentrations in shaping the CS, density, and TC. By adjusting ratios such as Na/Si and Na/Al, and optimizing NaOH molarity, properties can be tailored for specific requirements.
- Elemental and structural analyses, including EDS and XRD, confirm the formation of aluminosilicate gels and phases like C-A-S-H and C-S-H, which are integral to the material's mechanical properties and durability. The presence of phases like calcium carbonate, quartz, and larnite from SS and the amorphous characteristics of GGBS contribute to the reactivity and strength of the composite. This synergistic interaction between SS and GGBS phases results in enhanced mechanical properties and robustness of RuGPC, indicating the potential for tailored, high-performance geopolymer applications.
- FTIR spectroscopy of GGBS, SS, and SS-GGBS-based RuGPC composites reveals significant chemical and structural transformations during geopolymerization. Notable changes include the reduction of hydroxyl group vibration bands and the emergence of Si-O-Si and Si-O-Al bonds, indicating the development of a NASH gel and enhanced chemical bonding within the matrix. Additionally, as the percentage

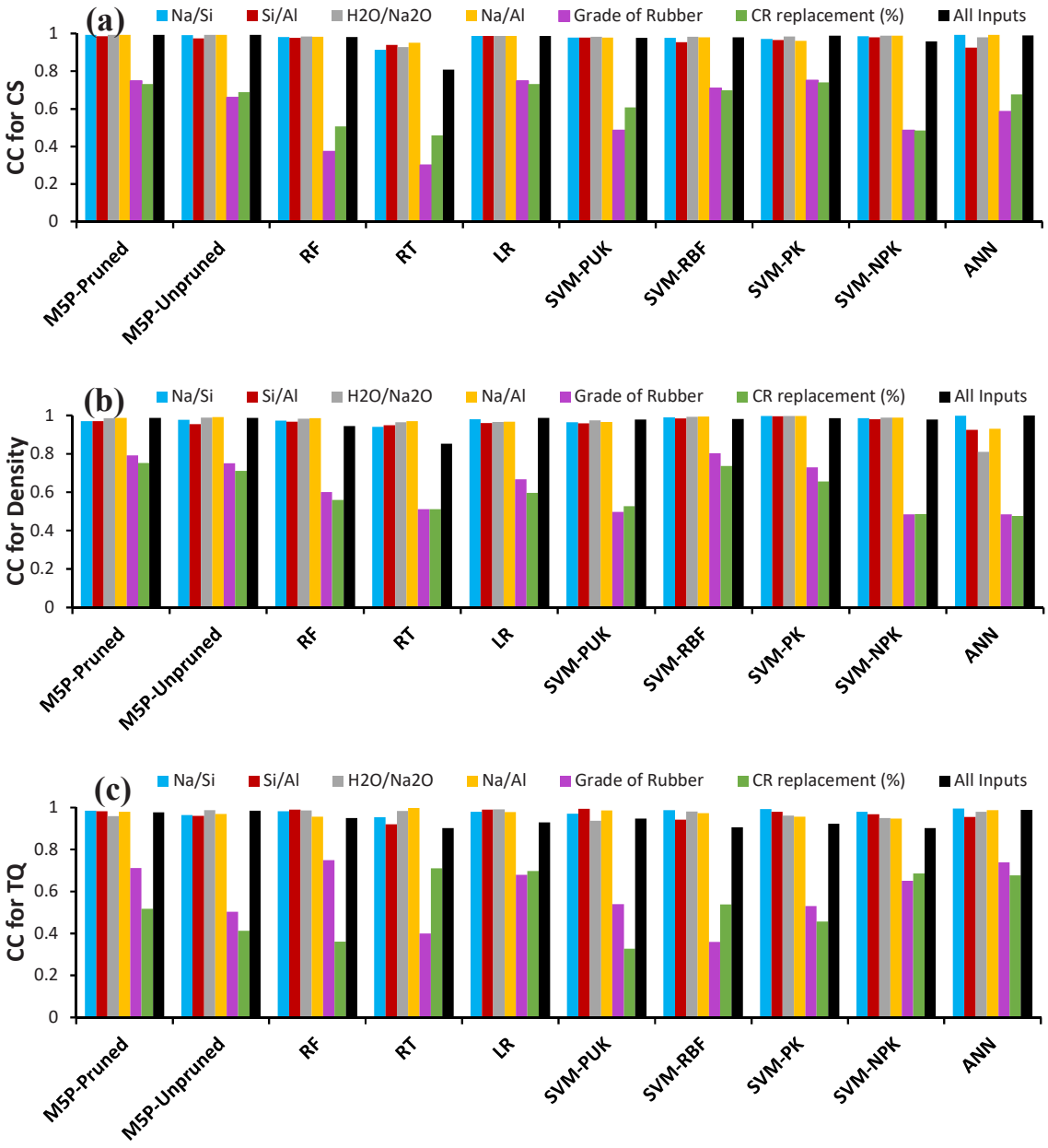

Fig. 24. Sensitivity Analysis of all models for (a) CS, (b) Density, and (c) TC.

Table 7
Cost analysis of RuGPC with four different Molarity concentrations (8 M, 10 M, 12 M, and 14 M).

Materials	Cost rate (Rs./kg)	M40 Mix (OPC 53-grade)		RuGPC (NaOH: M8)		RuGPC (NaOH: M10)		RuGPC (NaOH: M12)		RuGPC (NaOH: M14)	
		Quantity (kg/m^3)	Cost (Rs)	Quantity (kg/m^3)	Cost (Rs)	Quantity (kg/m^3)	Cost (Rs)	Quantity (kg/m^3)	Cost (Rs)	Quantity (kg/m^3)	Cost (Rs)
OPC	8.00	500.00	4000	-	-	-	-	-	-	-	-
GGBS	2.50	-	-	518.52	1296.30	518.52	1296.30	518.52	1296.30	518.52	1296.30
SS	2.50	-	-	518.52	1296.30	518.52	1296.30	518.52	1296.30	518.52	1296.30
Sand	1.50	683.00	1024.50	-	-	-	-	-	-	-	-
CD	0.56	-	-	311.11	173.52	311.11	173.52	311.11	173.52	311.11	173.52
Coarse aggregate	2.25	1289.00	2900.25	-	-	-	-	-	-	-	-
CR	10.10	-	-	133.33	1346.63	133.33	1346.63	133.33	1346.63	133.33	1346.63
Na_2SiO_3	10.00	-	-	370.37	3703.70	370.37	3703.70	370.37	3703.70	370.37	3703.70
NaOH Solid Content	10.05	-	-	38.84	390.34	46.29	465.21	53.45	537.17	60.57	608.73
Superplasticiser	15.00	26.67	400.05	-	-	-	-	-	-	-	-
Total cost (Rs.)			8324.80		8206.80		8281.67		8353.63		8425.19

of SS increases, further alterations lead to the formation of C-S-H gel, correlating directly with improvements in the material's strength properties.

- This study employed multiple ML techniques—including M5P, RF, RT, LR, SVM, and ANN—to predict the CS, density, and TC of RuGPC. Among these, ANN-based models excelled, showing superior predictive accuracy with high correlation coefficients and low error metrics (RMS, MAE, MAPE). The M5P models, both pruned and unpruned, also demonstrated exceptional performance, confirming their reliability and precision. Additionally, SVM-PUK models were particularly effective, meeting stringent performance criteria ideal for practical applications. Sensitivity analysis highlighted the grade of rubber as the most critical factor influencing predictions, with the percentage of CR replacement also significantly affecting outcomes. These insights underscore the potential of ML in enhancing decision-making in the construction industry, with specific model choices and parameter adjustments proving crucial for optimizing performance predictions.
- The findings of economic viability highlight significant cost savings achieved with RuGPC compared to traditional OPC-based materials, especially at a 10 % CR volume replacement with CD in 40:30:30 mixes in all Molarity concentrations. This demonstrates a promising advancement toward more economically viable and sustainable construction materials.

While the high-strength RuGPC developed in this study holds exhibits promising mechanical properties, durability, and economic advantages, much work is yet to be done on its complete realization for construction and infrastructure. Among major future research avenues that could be pursued is toughness enhancement and brittleness reduction in RuGPC, since improved ductility would extend its applicability regarding structural applications. Long-term performance studies, such as determination of creep, shrinkage, and fatigue resistance, would certainly provide more detailed insights into the material's behavior over time. Such aspects, if pursued in future studies, may open perspectives towards the generalization and robustness of RuGPC applications for a wide range of construction scenarios.

Ethical approval

All authors approve that the research was performed under all the ethical norms.

CRediT authorship contribution statement

Haytham F. Isleem: Writing – review & editing, Writing – original draft, Visualization, Validation, Resources, Methodology, Investigation, Funding acquisition, Formal analysis, Conceptualization. **Mohammed Rihan Maaze:** Writing – review & editing, Validation, Resources. **Ahmad Alyaseen:** Writing – review & editing, Writing – original draft, Visualization, Validation, Software, Resources, Methodology, Investigation, Formal analysis, Conceptualization. **Ashwin Narendra Raut:** Writing – review & editing, Writing – original draft, Resources, Project administration, Methodology, Formal analysis, Conceptualization. **Ahmed Salih Mohammed:** Writing – review & editing, Writing – original draft, Visualization, Validation, Resources. **Parveen Sihag:** Writing – review & editing, Visualization, Validation, Resources. **Afzal Husain Khan:** Writing – review & editing, Validation, Resources. **Arunava Poddar:** Writing – review & editing, Writing – original draft, Visualization.

Declaration of Competing Interest

The authors declare that they have no known competing financial interests or personal relationships that could have appeared to influence the work reported in this paper.

Appendix A. Supporting information

Supplementary data associated with this article can be found in the online version at doi:10.1016/j.conbuildmat.2024.138985.

Data Availability

Data will be made available on request.

References

[1] T.R. Naik, Sustainability of concrete construction, Pract. Period. Struct. Des. Constr. 13 (2008) 98–103, https://doi.org/10.1061/(ASCE)1084-0680(2008)13:2(98).
[2] A. Adesina, Recent advances in the concrete industry to reduce its carbon dioxide emissions, Environ. Chall. 1 (2020) 100004, https://doi.org/10.1016/j.envc.2020.100004.
[3] C. Meyer, The greening of the concrete industry, Cem. Concr. Compos 31 (2009) 601–605, https://doi.org/10.1016/j.cemconcomp.2008.12.010.
[4] M. Amran, A. Al-Fakih, S.H. Chu, R. Fediuk, S. Haruna, A. Azevedo, N. Vatin, Long-term durability properties of geopolymer concrete: An in-depth review, Case Stud. Constr. Mater. 15 (2021) e00661, https://doi.org/10.1016/j.cscm.2021.e00661.
[5] N. Shehata, O.A. Mohamed, E.T. Sayed, M.A. Abdelkareem, A.G. Olabi, Geopolymer concrete as green building materials: Recent applications, sustainable development and circular economy potentials, Sci. Total Environ. 836 (2022) 155577, https://doi.org/10.1016/j.scitotenv.2022.155577.
[6] D.M. González-García, L. Téllez-Jurado, F.J. Jiménez-Álvarez, L. Zarazua-Villalobos, H. Balmori-Ramírez, Evolution of a natural pozzolan-based geopolymer alkalized in the presence of sodium or potassium silicate/hydroxide solution, Constr. Build. Mater. 321 (2022) 126305, https://doi.org/10.1016/j.conbuildmat.2021.126305.
[7] J. Zhao, L. Tong, B. Li, T. Chen, C. Wang, G. Yang, Y. Zheng, Eco-friendly geopolymer materials: A review of performance improvement, potential application and sustainability assessment, J. Clean. Prod. 307 (2021) 127085, https://doi.org/10.1016/j.jclepro.2021.127085.
[8] J.J. Biernacki, J.W. Bullard, G. Sant, K. Brown, F.P. Glasser, S. Jones, T. Ley, R. Livingston, L. Nicoleau, J. Olek, F. Sanchez, R. Shahsavari, P.E. Stutzman, K. Sobolev, T. Prater, CemEnts In The 21 St Century: Challenges, Perspectives, And Opportunities, J. Am. Ceram. Soc. 100 (2017) 2746–2773, https://doi.org/10.1111/jace.14948.
[9] T. Hanein, J.-L. Galvez-Martos, M.N. Bannerman, Carbon footprint of calcium sulfoaluminate clinker production, J. Clean. Prod. 172 (2018) 2278–2287, https://doi.org/10.1016/j.jclepro.2017.11.183.
[10] J. Min, G. Yan, A.M. Abed, S. Elattar, M. Amine Khadimallah, A. Jan, H. Elhosiny Ali, The effect of carbon dioxide emissions on the building energy efficiency, Fuel 326 (2022) 124842, https://doi.org/10.1016/j.fuel.2022.124842.
[11] B. Kanagaraj, N. Anand, S. Raj R, E. Lubloy, Performance evaluation of sodium silicate waste as a replacement for conventional sand in geopolymer concrete, J. Clean. Prod. 375 (2022) 134172, https://doi.org/10.1016/j.jclepro.2022.134172.
[12] S. Luhar, I. Luhar, R. Gupta, Durability performance evaluation of green geopolymer concrete, Eur. J. Environ. Civ. Eng. 26 (2022) 4297–4345, https://doi.org/10.1080/19648189.2020.1847691.
[13] A.N. Raut, M. Adamu, V.C. Khed, A.L. Murmu, Y.E. Ibrahim, Effects of agro-industrial by-products as alumina-silicate source on the mechanical and thermal properties of fly ash based-alkali activated binder, Case Stud. Constr. Mater. 18 (2023) e02070, https://doi.org/10.1016/j.cscm.2023.e02070.
[14] A.N. Raut, A.L. Murmu, T. Alomayri, Physico-mechanical and thermal behavior of prolong heat cured geopolymer blocks, Constr. Build. Mater. 370 (2023) 130309, https://doi.org/10.1016/j.conbuildmat.2023.130309.
[15] J. Liu, P. Tran, Cement mortar containing crumb rubber coated with geopolymer: From microstructural properties to compressive strength, Constr. Build. Mater. 383 (2023) 131284, https://doi.org/10.1016/j.conbuildmat.2023.131284.
[16] P. Gill, P. Jangra, R. Roychand, M. Saberian, J. Li, Effects of various additives on the crumb rubber integrated geopolymer concrete, Clean. Mater. 8 (2023) 100181, https://doi.org/10.1016/j.clema.2023.100181.
[17] M. Elzeadani, D.V. Bompa, A.Y. Elghazouli, Preparation and properties of rubberised geopolymer concrete: A review, Constr. Build. Mater. 313 (2021) 125504, https://doi.org/10.1016/j.conbuildmat.2021.125504.
[18] Y. Park, A. Abolmaali, Y.H. Kim, M. Ghahremannejad, Compressive strength of fly ash-based geopolymer concrete with crumb rubber partially replacing sand, Constr. Build. Mater. 118 (2016) 43–51, https://doi.org/10.1016/j.conbuildmat.2016.05.001.
[19] A.A. Azmi, M.M.A.B. Abdullah, C.M.R. Ghazali, A. Victor Sandu, K. Hussin, Effect Of crumb rubber on compressive strength of fly ash based geopolymer concrete, MATEC Web Conf. 78 (2016) 01063, https://doi.org/10.1051/matecconf/20167801063.
[20] M. Gandoman, M. Kokabi, Sound barrier properties of sustainable waste rubber/geopolymer concretes, Iran. Polym. J. 24 (2015) 105–112, https://doi.org/10.1007/s13726-014-0304-1.

[21] S. Luhar, S. Chaudhary, I. Luhar, Development of rubberized geopolymer concrete: Strength and durability studies, Constr. Build. Mater. 204 (2019) 740–753, https://doi.org/10.1016/j.conbuildmat.2019.01.185.
[22] A.M. Aly, M.S. El-Feky, M. Kohail, E.-S.A.R. Nasr, Performance of geopolymer concrete containing recycled rubber, Constr. Build. Mater. 207 (2019) 136–144, https://doi.org/10.1016/j.conbuildmat.2019.02.121.
[23] A. Wongsa, V. Sata, B. Nematollahi, J. Sanjayan, P. Chindaprasirt, Mechanical and thermal properties of lightweight geopolymer mortar incorporating crumb rubber, J. Clean. Prod. 195 (2018) 1069–1080, https://doi.org/10.1016/j.jclepro.2018.06.003.
[24] J. Liu, S. Setunge, P. Tran, 3D concrete printing with cement-coated recycled crumb rubber: Compressive and microstructural properties, Constr. Build. Mater. 347 (2022) 128507, https://doi.org/10.1016/j.conbuildmat.2022.128507.
[25] Y. Wang, T. Zheng, X. Zheng, Y. Liu, J. Darkwa, G. Zhou, Thermo-mechanical and moisture absorption properties of fly ash-based lightweight geopolymer concrete reinforced by polypropylene fibers, Constr. Build. Mater. 251 (2020) 118960, https://doi.org/10.1016/j.conbuildmat.2020.118960.
[26] A. Benazzouk, O. Douzane, K. Mezreb, B. Laidoudi, M. Quéneudec, Thermal conductivity of cement composites containing rubber waste particles: experimental study and modelling, Constr. Build. Mater. 22 (2008) 573–579, https://doi.org/10.1016/j.conbuildmat.2006.11.011.
[27] A. Cojocaru, D.N. Isopescu, S.G. Maxineasa, S.G. Petre, Assessment of Thermal and Mechanical Properties of Cement-Based Materials—Part 1: Crumb Rubber Concrete, Buildings 13 (2023) 324, https://doi.org/10.3390/buildings13020324.
[28] A.M. Rashad, A comprehensive overview about recycling rubber as fine aggregate replacement in traditional cementitious materials, Int. J. Sustain. Built Environ. 5 (2016) 46–82, https://doi.org/10.1016/j.ijsbe.2015.11.003.
[29] O. Youssf, M. Elchalakani, R. Hassanli, R. Roychand, Y. Zhuge, R.J. Gravina, J. E. Mills, Mechanical performance and durability of geopolymer lightweight rubber concrete, J. Build. Eng. 45 (2022) 103608, https://doi.org/10.1016/j.jobe.2021.103608.
[30] W.K. Part, M. Ramli, C.B. Cheah, An overview on the influence of various factors on the properties of geopolymer concrete derived from industrial by-products, Constr. Build. Mater. 77 (2015) 370–395, https://doi.org/10.1016/j.conbuildmat.2014.12.065.
[31] H. Xu, W. Gong, L. Syltebo, K. Izzo, W. Lutze, I.L. Pegg, Effect of blast furnace slag grades on fly ash based geopolymer waste forms, Fuel 133 (2014) 332–340, https://doi.org/10.1016/j.fuel.2014.05.018.
[32] P.S. Deb, P. Nath, P.K. Sarker, The effects of ground granulated blast-furnace slag blending with fly ash and activator content on the workability and strength properties of geopolymer concrete cured at ambient temperature, Mater. Des. (1980-2015) 62 (2014) 32–39, https://doi.org/10.1016/j.matdes.2014.05.001.
[33] A. Islam, U.J. Alengaram, M.Z. Jumaat, I.I. Bashar, The development of compressive strength of ground granulated blast furnace slag-palm oil fuel ash-fly ash based geopolymer mortar, Mater. Des. (1980-2015) 56 (2014) 833–841, https://doi.org/10.1016/j.matdes.2013.11.080.
[34] G. Kürklü, The effect of high temperature on the design of blast furnace slag and coarse fly ash-based geopolymer mortar, Compos B Eng. 92 (2016) 9–18, https://doi.org/10.1016/j.compositesb.2016.02.043.
[35] P. Duxson, A. Fernández-Jiménez, J.L. Provis, G.C. Lukey, A. Palomo, J.S.J. van Deventer, Geopolymer technology: the current state of the art, J. Mater. Sci. 42 (2007) 2917–2933, https://doi.org/10.1007/s10853-006-0637-z.
[36] B.S. Thomas, R.C. Gupta, A comprehensive review on the applications of waste tire rubber in cement concrete, Renew. Sustain. Energy Rev. 54 (2016) 1323–1333, https://doi.org/10.1016/j.rser.2015.10.092.
[37] A. Özbayrak, H. Kucukgoncu, H.H. Aslanbay, Y.G. Aslanbay, O. Atas, Comprehensive experimental analysis of the effects of elevated temperatures in geopolymer concretes with variable alkali activator ratios, J. Build. Eng. 68 (2023) 106108, https://doi.org/10.1016/j.jobe.2023.106108.
[38] S. Nagajothi, S. Elavenil, Effect of GGBS Addition on Reactivity and Microstructure Properties of Ambient Cured Fly Ash Based Geopolymer Concrete, Silicon 13 (2021) 507–516, https://doi.org/10.1007/s12633-020-00470-w.
[39] J.L. Provis, S.A. Bernal, Geopolymers and Related Alkali-Activated Materials, Annu Rev. Mater. Res 44 (2014) 299–327, https://doi.org/10.1146/annurev-matsci-070813-113515.
[40] J. Temuujin, A. van Riessen, R. Williams, Influence of calcium compounds on the mechanical properties of fly ash geopolymer pastes, J. Hazard Mater. 167 (2009) 82–88, https://doi.org/10.1016/j.jhazmat.2008.12.121.
[41] M. Nodehi, V.M. Taghvaee, Alkali-activated materials and geopolymer: a review of common precursors and activators addressing circular economy, Circ. Econ. Sustain. 2 (2022) 165–196, https://doi.org/10.1007/s43615-021-00029-w.
[42] I. Garcia-Lodeiro, A. Palomo, A. Fernández-Jiménez, An overview of the chemistry of alkali-activated cement-based binders. in: Handbook of Alkali-Activated Cements, Mortars and Concretes, Elsevier, 2015, pp. 19–47, https://doi.org/10.1533/9781782422884.1.19.
[43] J.L. Provis, J.S.J. van Deventer, Geopolymers, Woodhead Publishing Limited, 2009, https://doi.org/10.1533/9781845696382.
[44] J.L. Provis, S.A. Bernal, Bind. Chem. – Blended Syst. Intermed. Ca Content (2014) 125–144, https://doi.org/10.1007/978-94-007-7672-2_5.
[45] A.B. Malkawi, M.F. Nuruddin, A. Fauzi, H. Almattarneh, B.S. Mohammed, Effects of Alkaline Solution on Properties of the HCFA Geopolymer Mortars, Procedia Eng. 148 (2016) 710–717, https://doi.org/10.1016/j.proeng.2016.06.581.
[46] B. Pratap, S. Mondal, B. Hanumantha Rao, NaOH molarity influence on mechanical and durability properties of geopolymer concrete made with fly ash and phosphogypsum, Structures 56 (2023) 105035, https://doi.org/10.1016/j.istruc.2023.105035.
[47] N. Ranjbar, M. Mehrali, A. Behnia, U.J. Alengaram, M.Z. Jumaat, Compressive strength and microstructural analysis of fly ash/palm oil fuel ash based geopolymer mortar, Mater. Des. 59 (2014) 532–539, https://doi.org/10.1016/j.matdes.2014.03.037.
[48] A. Nazari, A. Bagheri, S. Riahi, Properties of geopolymer with seeded fly ash and rice husk bark ash, Mater. Sci. Eng.: A 528 (2011) 7395–7401, https://doi.org/10.1016/j.msea.2011.06.027.
[49] X. Guo, H. Shi, W.A. Dick, Compressive strength and microstructural characteristics of class C fly ash geopolymer, Cem. Concr. Compos 32 (2010) 142–147, https://doi.org/10.1016/j.cemconcomp.2009.11.003.
[50] S.K. Nath, S. Kumar, Influence of iron making slags on strength and microstructure of fly ash geopolymer, Constr. Build. Mater. 38 (2013) 924–930, https://doi.org/10.1016/j.conbuildmat.2012.09.070.
[51] B. Ma, Z. Zhu, W. Huo, L. Yang, Y. Zhang, H. Sun, X. Zhang, Assessing the viability of a high performance one-part geopolymer made from fly ash and GGBS at ambient temperature, J. Build. Eng. 75 (2023) 106978, https://doi.org/10.1016/j.jobe.2023.106978.
[52] F. Aslani, G. Ma, D.L. Yim Wan, G. Muselin, Development of high-performance self-compacting concrete using waste recycled concrete aggregates and rubber granules, J. Clean. Prod. 182 (2018) 553–566, https://doi.org/10.1016/j.jclepro.2018.02.074.
[53] A.N. Raut, A. Alyaseen, A.H. Khan, S. Janga, A. Poddar, P. Sihag, V. Sumra, D. Lee, R. Kumar, T. Singh, Incorporating crumb rubber in slag-based geopolymer: Experimental work and predictive modelling, Case Studies in Construction Materials 21 (2024) e03893, https://doi.org/10.1016/j.cscm.2024.e03893.
[54] P. He, B. Zhang, J.-X. Lu, C.S. Poon, Reaction mechanisms of alkali-activated glass powder-ggbs-CAC composites, Cem. Concr. Compos 122 (2021) 104143, https://doi.org/10.1016/j.cemconcomp.2021.104143.
[55] H.L. Dinh, J. Liu, J.-H. Doh, D.E.L. Ong, Influence of Si/Al molar ratio and ca content on the performance of fly ash-based geopolymer incorporating waste glass and GGBFS, Constr. Build. Mater. 411 (2024) 134741, https://doi.org/10.1016/j.conbuildmat.2023.134741.
[56] A. Nmiri, M. Duc, N. Hamdi, O. Yazoghli-Marzouk, E. Srasra, Replacement of alkali silicate solution with silica fume in metakaolin-based geopolymers, Int. J. Miner., Metall., Mater. 26 (2019) 555–564, https://doi.org/10.1007/s12613-019-1764-2.
[57] H. Castillo, H. Collado, T. Droguett, S. Sánchez, M. Vesely, P. Garrido, S. Palma, Factors Affecting the Compressive Strength of Geopolymers: A Review, Minerals 11 (2021) 1317, https://doi.org/10.3390/min11121317.
[58] H. Yong-Jie, H. Cheng-Yong, L. Yun-Ming, M.M. Al Bakri Abdullah, L. Yeng-Seng, K. Ern-Hun, O. Shee-Ween, O. Wan-En, N. Hui-Teng, N. Yong-Sing, Strength optimization and key factors correlation of one-part fly ash/ladle furnace slag (FA/LFS) geopolymer using statistical approach, J. Build. Eng. 63 (2023) 105480, https://doi.org/10.1016/j.jobe.2022.105480.
[59] H.A. Ali, K. Sun, D. Xuan, J.-X. Lu, M. Cyr, C.S. Poon, Recycling of high-volume waste glass powder in alkali-activated materials: an efflorescence mitigation strategy, J. Build. Eng. 65 (2023) 105756, https://doi.org/10.1016/j.jobe.2022.105756.
[60] A. Gholampour, A. Memarzadeh, M. Nematzadeh, M. Valizadeh Kiamahalleh, T. D. Ngo, Concrete containing recycled concrete coarse aggregate and crushed glass sand: <scp>Mitigating</scp> the effect of alkali–silica reaction, Struct. Concr. (2024), https://doi.org/10.1002/suco.202301029.
[61] J. Sengupta, N. Dhang, A. Deb, Efficient mix design of one-part alkali-activated concrete using packing density method and its optimization through Taguchi-GRA, Constr. Build. Mater. 438 (2024) 136869, https://doi.org/10.1016/j.conbuildmat.2024.136869.
[62] A.Haris Subaer, A. Nurhayati, J.J.Ekaputri Irhamsyah, The Influence of Si:Al and Na:Al on the physical and microstructure characters of geopolymers based on metakaolin, Mater. Sci. Forum 841 (2016) 170–177, https://doi.org/10.4028/www.scientific.net/MSF.841.170.
[63] R. He, N. Dai, Z. Wang, Thermal and Mechanical Properties of Geopolymers Exposed to High Temperature: A Literature Review, Adv. Civ. Eng. 2020 (2020) 1–17, https://doi.org/10.1155/2020/7532703.
[64] G. Liang, H. Zhu, Z. Zhang, Q. Wu, Effect of rice husk ash addition on the compressive strength and thermal stability of metakaolin based geopolymer, Constr. Build. Mater. 222 (2019) 872–881, https://doi.org/10.1016/j.conbuildmat.2019.06.200.
[65] I. G, B. Singh, S. Deshwal, S.K. Bhattacharyya, Effect of sodium carbonate/sodium silicate activator on the rheology, geopolymerization and strength of fly ash/slag geopolymer pastes, Cem. Concr. Compos 97 (2019) 226–238, https://doi.org/10.1016/j.cemconcomp.2018.12.007.
[66] A. Saludung, T. Azeyanagi, Y. Ogawa, K. Kawai, Effect of silica fume on efflorescence formation and alkali leaching of alkali-activated slag, J. Clean. Prod. 315 (2021) 128210, https://doi.org/10.1016/j.jclepro.2021.128210.
[67] Y. Wang, X. Liu, W. Zhang, Z. Li, Y. Zhang, Y. Li, Y. Ren, Effects of Si/Al ratio on the efflorescence and properties of fly ash based geopolymer, J. Clean. Prod. 244 (2020) 118852, https://doi.org/10.1016/j.jclepro.2019.118852.
[68] F. Puertas, M. Palacios, H. Manzano, J.S. Dolado, A. Rico, J. Rodriguez, C-A-S-H gels formed in alkali-activated slag cement pastes. Structure and effect on cement properties and durability, MATEC Web Conf. 11 (2014) 01002, https://doi.org/10.1051/matecconf/20141101002.
[69] N.J. Clayden, S. Esposito, A. Aronne, P. Pernice, Solid state 27Al NMR and FTIR study of lanthanum aluminosilicate glasses, J. Non Cryst. Solids 258 (1999) 11–19, https://doi.org/10.1016/S0022-3093(99)00555-4.

[70] G. Lecomte-Nana, H. Goure-Doubi, A. Smith, A. Wattiaux, G. Lecomte, Effect of iron phase on the strengthening of lateritic-based "geomimetic" materials, Appl. Clay Sci. 70 (2012) 14–21, https://doi.org/10.1016/j.clay.2012.09.014.
[71] A. Nana, J. Ngouné, R.C. Kaze, L. Boubakar, S.K. Tchounang, H.K. Tchakouté, E. Kamseu, C. Leonelli, Room-temperature alkaline activation of feldspathic solid solutions: Development of high strength geopolymers, Constr. Build. Mater. 195 (2019) 258–268, https://doi.org/10.1016/j.conbuildmat.2018.11.068.
[72] Y, W.I.H. Wang, Inducing model trees for continuous classes, Ninth Eur. Conf. Mach. Learn. (1997) 128–137.
[73] J.R. Quinlan, Learning with continuous classes, : 5th Aust. Jt. Conf. Artif. Intell. (1992) 343–348.
[74] D. Puri, R. Kumar, S. Kumar, M.S. Thakur, G. Fekete, D. Lee, T. Singh, Performance analysis and modelling of circular jets aeration in an open channel using soft computing techniques, Sci. Rep. 14 (2024) 3140, https://doi.org/10.1038/s41598-024-53407-3.
[75] Y. Yu, T.N. Nguyen, J. Li, L.F.M. Sanchez, A. Nguyen, Predicting elastic modulus degradation of alkali silica reaction affected concrete using soft computing techniques: a comparative study, Constr. Build. Mater. 274 (2021) 122024, https://doi.org/10.1016/j.conbuildmat.2020.122024.
[76] X. Chen, H. Ishwaran, Random forests for genomic data analysis, Genomics 99 (2012) 323–329, https://doi.org/10.1016/j.ygeno.2012.04.003.
[77] D. Puri, D. Lee, D.V. khankal, M.S. Thakur, F.M. Alfaisal, S. Alam, R. Kumar, M. A. Khan, Decision tree-based modeling of the aeration effectiveness of circular plunging jets, ACS Omega 8 (2023) 38950–38960, https://doi.org/10.1021/acsomega.3c03375.
[78] S. Gupta, P. Sihag, Prediction of the compressive strength of concrete using various predictive modeling techniques, Neural Comput. Appl. 34 (2022) 6535–6545, https://doi.org/10.1007/s00521-021-06820-y.
[79] P. Geurts, D. Ernst, L. Wehenkel, Extremely randomized trees, Mach. Learn 63 (2006) 3–42, https://doi.org/10.1007/s10994-006-6226-1.
[80] W. Fan, J. McCloskey, P.S. Yu, A general framework for accurate and fast regression by data summarization in random decision trees. in: Proceedings of the 12th ACM SIGKDD International Conference on Knowledge Discovery and Data Mining, ACM, New York, NY, USA, 2006, pp. 136–146, https://doi.org/10.1145/1150402.1150421.
[81] F. Almohammed, M.S. Thakur, D. Lee, R. Kumar, T. Singh, Flexural and split tensile strength of concrete with basalt fiber: an experimental and computational analysis, Constr. Build. Mater. 414 (2024) 134936, https://doi.org/10.1016/j.conbuildmat.2024.134936.
[82] I. Gonçalves, S. Silva, J.B. Melo, J.M.B. Carreiras, Random Sampl. Tech. Overfitting Control Genet. Program. (2012) 218–229, https://doi.org/10.1007/978-3-642-29139-5_19.
[83] J. Neter, M.H. Kutner, C.J. Nachtsheim, W. Wasserman, Appl. Linear Stat. Models (1996).
[84] M.H. Kutner, C.J. Nachtsheim, J. Neter, W. Li. Applied linear statistical models, Fifth Edition, McGraw-hill, 2005.
[85] S. Ding, Z. Zhu, X. Zhang, An overview on semi-supervised support vector machine, Neural Comput. Appl. 28 (2017) 969–978, https://doi.org/10.1007/s00521-015-2113-7.
[86] S. Suthaharan, Support Vector Mach. (2016) 207–235, https://doi.org/10.1007/978-1-4899-7641-3_9.
[87] M. Yazdani, M. Babagolzadeh, N. Kazemitash, M. Saberi, Reliability estimation using an integrated support vector regression – variable neighborhood search model, J. Ind. Inf. Integr. 15 (2019) 103–110, https://doi.org/10.1016/j.jii.2019.03.001.
[88] A. Kandiri, E. Mohammadi Golafshani, A. Behnood, Estimation of the compressive strength of concretes containing ground granulated blast furnace slag using hybridized multi-objective ANN and salp swarm algorithm, Constr. Build. Mater. 248 (2020) 118676, https://doi.org/10.1016/j.conbuildmat.2020.118676.
[89] B. Cai, G. Pan, F. Fu, Prediction of the Postfire Flexural Capacity of RC Beam Using GA-BPNN Machine Learning, J. Perform. Constr. Facil. 34 (2020), https://doi.org/10.1061/(ASCE)CF.1943-5509.0001514.
[90] F. Fu, Fire induced progressive collapse potential assessment of steel framed buildings using machine learning, J. Constr. Steel Res 166 (2020) 105918, https://doi.org/10.1016/j.jcsr.2019.105918.
[91] P. Kumari, S. Paruthi, A. Alyaseen, A. Husain Khan, A. Jijja, Predictive performance assessment of recycled coarse aggregate concrete using artificial intelligence: A review, Clean. Mater. 13 (2024) 100263, https://doi.org/10.1016/j.clema.2024.100263.
[92] B. Cai, L.-F. Xu, F. Fu, Shear Resistance Prediction of Post-fire Reinforced Concrete Beams Using Artificial Neural Network, Int J. Concr. Struct. Mater. 13 (2019) 46, https://doi.org/10.1186/s40069-019-0358-8.
[93] A.A. Shahmansouri, M. Yazdani, S. Ghanbari, H. Akbarzadeh Bengar, A. Jafari, H. Farrokh Ghatte, Artificial neural network model to predict the compressive strength of eco-friendly geopolymer concrete incorporating silica fume and natural zeolite, J. Clean. Prod. 279 (2021) 123697, https://doi.org/10.1016/j.jclepro.2020.123697.
[94] M. Rahmati, V. Toufigh, Evaluation of geopolymer concrete at high temperatures: An experimental study using machine learning, J. Clean. Prod. 372 (2022) 133608, https://doi.org/10.1016/j.jclepro.2022.133608.
[95] A. Alyaseen, A. Poddar, H. Alahmad, N. Kumar, P. Sihag, High-performance self-compacting concrete with recycled coarse aggregate: comprehensive systematic review on mix design parameters, J. Struct. Integr. Maint. (2023) 1–18, https://doi.org/10.1080/24705314.2023.2211850.
[96] A. Alyaseen, A. Poddar, N. Kumar, P. Sihag, D. Lee, R. kumar, T. Singh, Assessing the compressive and splitting tensile strength of self-compacting recycled coarse aggregate concrete using machine learning and statistical techniques, Mater. Today Commun. 38 (2024) 107970, https://doi.org/10.1016/j.mtcomm.2023.107970.
[97] A. Alyaseen, A. Poddar, N. Kumar, S. Tajjour, C.V.S.R. Prasad, H. Alahmad, P. Sihag, High-performance self-compacting concrete with recycled coarse aggregate: soft-computing analysis of compressive strength, J. Build. Eng. 77 (2023) 107527, https://doi.org/10.1016/j.jobe.2023.107527.
[98] A. Alyaseen, C.V. Siva Rama Prasad, A. Poddar, N. Kumar, R.R. Mostafa, F. Almohammed, P. Sihag, Application of soft computing techniques for the prediction of splitting tensile strength in bacterial concrete, J. Struct. Integr. Maint. 8 (2023) 26–35, https://doi.org/10.1080/24705314.2022.2142900.
[99] A. Alyaseen, A. Poddar, N. Kumar, K. Haydar, A. Khan, P. Sihag, D. Lee, R. Kumar, T. Singh, Influence of silica fume and Bacillus subtilis combination on concrete made with recycled concrete aggregate: experimental investigation, economic analysis, and machine learning modeling, Case Stud. Constr. Mater. 19 (2023) e02638, https://doi.org/10.1016/j.cscm.2023.e02638.
[100] V. Kashyap, A. Alyaseen, A. Poddar, Supervised and unsupervised machine learning techniques for predicting mechanical properties of coconut fiber reinforced concrete, Asian J. Civ. Eng. (2024), https://doi.org/10.1007/s42107-024-01018-8.
[101] R. Alzein, M.V. Kumar, A.N. Raut, A. Alyaseen, P. Sihag, D. Lee, R. Kumar, T. Singh, Polypropylene waste plastic fiber morphology as an influencing factor on the performance and durability of concrete: experimental investigation, soft-computing modeling, and economic analysis, Constr. Build. Mater. 438 (2024) 137244, https://doi.org/10.1016/j.conbuildmat.2024.137244.
[102] H. Verbeeck, R. Samson, F. Verdonck, R. Lemeur, Parameter sensitivity and uncertainty of the forest carbon flux model FORUG: a Monte Carlo analysis, Tree Physiol. 26 (2006) 807–817, https://doi.org/10.1093/treephys/26.6.807.
[103] J, D.S. Thaarrini, Comparative study on the production cost of geopolymer and conventional concretes, Int. J. Civ. Eng. Res. 7 (2016) 117–124.
[104] B.C. McLellan, R.P. Williams, J. Lay, A. van Riessen, G.D. Corder, Costs and carbon emissions for geopolymer pastes in comparison to ordinary portland cement, J. Clean. Prod. 19 (2011) 1080–1090, https://doi.org/10.1016/j.jclepro.2011.02.010.
[105] B.J, S.M, N.C. Mathew, Strength, economic and sustainability characteristics of coal ash–GGBS based geopolymer concrete, Int. J. Comput. Eng. Res 3 (2013) 207–212.
[106] J.O. Ikotun, G.E. Aderinto, M.M. Madirisha, V.Y. Katte, Geopolymer cement in pavement applications: bridging sustainability and performance, Sustainability 16 (2024) 5417, https://doi.org/10.3390/su16135417.
[107] S. Saha, D. Sau, T. Hazra, Economic viability analysis of recycling waste plastic as aggregates in green sustainable concrete, Waste Manag. 169 (2023) 289–300, https://doi.org/10.1016/j.wasman.2023.07.023.
[108] S. Luhar, S. Chaudhary, I. Luhar, Development of rubberized geopolymer concrete: strength and durability studies, Constr. Build. Mater. 204 (2019) 740–753, https://doi.org/10.1016/j.conbuildmat.2019.01.185.